

# Chapter 2

## Modeling and Analysis of Desiccant Wheel

Jae Dong Chung

**Abstract** Desiccant cooling systems have advantages in environmentally friendly operation and separate control of sensible and latent cooling loads, which leads to comfortable indoor air quality. In addition, the desiccant cooling system is a heat-driven cycle and therefore has the ability to use low-grade energy. However, the wide spread use of this technology is not yet possible due to its relatively large size and low system performance. The wheel is the most crucial component of the desiccant cooling system. Therefore, mathematical modeling of the desiccant wheel plays an important role in enhancing the overall system performance. Heat and mass transfer are coupled, and multiple parameters are involved in understanding the complicated phenomena in desiccant wheels. Mathematical models are commonly accepted as an effective method for analyzing the performance of rotary wheels and systems. The models can also be used to guide system operation, interpret experimental results and assist in system design and optimization. Several mathematical models have been constructed and employed to analyze, develop and design desiccant wheels. In this work, a brief review on the mathematical modeling of the desiccant wheel is examined, and some typical issues and results of case studies are discussed.

**Keywords** Desiccant wheel • Numerical analysis • Parametric study • Optimization • Isotherm

### Nomenclature

$a$	Channel height (m)
$A$	Area ( $\text{m}^2$ )
$b$	Channel width (m)
$BP$	Rate of outdoor influx

---

J.D. Chung (✉)  
Mechanical Engineering, Sejong University, Seoul 05006, Korea  
e-mail: jdchung@sejong.ac.kr

© Springer Nature Singapore Pte Ltd. 2017  
N. Enteria et al. (eds.), *Desiccant Heating, Ventilating,  
and Air-Conditioning Systems*, DOI 10.1007/978-981-10-3047-5\_2

$c$	Channel wall thickness (m)
$c_p$	Specific heat of dry air water ( $\text{J kg}^{-1} \text{K}^{-1}$ )
COP	Coefficient of performance
$D_G$	Effective gas phase diffusivity ( $\text{m}^2 \text{s}^{-1}$ )
$D_h$	Hydraulic diameter (m)
$D_K$	Knudsen diffusivity ( $\text{m}^2 \text{s}^{-1}$ )
$D_S$	Surface diffusivity ( $\text{m}^2 \text{s}^{-1}$ )
$D_{so}$	Pre-exponent constant of surface diffusivity, $\text{m}^2 \text{s}^{-1}$
$E_a$	Activation energy of diffusion, $\text{J mol}^{-1}$
$f$	Mass fraction of desiccant in the wheel
$f_m$	Mass fraction of desiccant in the wheel
$F_0$	Ratio of mean squares of factor $i$ to error
$H$	Enthalpy ( $\text{J kg}^{-1}$ )
$H_{sor}$	Heat of adsorption ( $\text{J kg}^{-1}$ )
$h$	Convective heat transfer coefficient ( $\text{W m}^{-2} \text{K}^{-1}$ )
$h_m$	Mass transfer coefficient ( $\text{kg m}^{-2} \text{s}^{-1}$ )
$K_y$	Gas-side mass transfer coefficient ( $\text{kg m}^2 \text{s}$ )
$k$	Thermal conductivity ( $\text{W m}^{-1} \text{K}^{-1}$ )
$L$	Channel length (m)
$Le$	Lewis number
$N$	Number of experiment
$\dot{m}$	Mass flow rate ( $\text{kg h}^{-1}$ )
MRC	Moisture removal capacity ( $\text{kg h}^{-1}$ )
Nu	Nusselt number, $hD_h/k_a$
$P$	Perimeter of flow channel (m)
$P, P_s$	Pressure, saturated pressure (Pa)
$Q$	Cooling capacity per unit air flow rate ( $\text{J kg}^{-1}$ )
$q^*$	Equilibrium water uptake, $\text{kg kg}^{-1}$
$r$	Radial coordinate
$R_u$	Universal gas constant, $\text{J K}^{-1} \text{mol}^{-1}$
$R_v$	Gas constant of vapor, $\text{JK}^{-1} \text{kg}^{-1}$
$R$	Separate factor
$ST$	Sum of square of experiment
$t$	Time (s)
$T$	Temperature ( $^{\circ}\text{C}$ )
$u$	Velocity ( $\text{m s}^{-1}$ )
$V$	Mean square
$W$	Water content of the desiccant material ( $\text{kg kg}^{-1}$ )
$W_{\max}$	Maximum humidity ration of dry air ( $\text{kg kg}^{-1}$ )
$Y$	Humidity ratio ( $\text{kg kg}^{-1}$ )
$z$	Axial coordinate (m)

**Greek letters**

$\alpha$	Significance level
$\alpha^*$	Dimensionless channel area ration, $a/b$
$\varepsilon$	Performance
$\varepsilon_d$	Wheel effectiveness
$\varphi$	Humidity ratio or degree of freedom
$\gamma$	Isothermal curve gradient of a linear model
$\theta$	Angular coordinate
$\rho$	Density ( $\text{kg m}^{-3}$ )
$\tau$	Tortuosity

**Subscripts**

1, 2, 3	Levels
a	Air
ad	Air in desiccant pore
d	Desiccant
e	Error
h	Hot
H	Constant heat flux
in	Inlet
l	Liquid
out	Outlet
p	Process
r	Regeneration
REC	Regenerative evaporative cooler
SHE	Sensible heat exchanger
T	Constant temperature
v	Vapor
w	Desiccant

**2.1 Introduction**

The design of heating, ventilating and air-conditioning (HVAC) systems for thermal comfort requires increasing attention, particularly to matters arising from recent regulations and standards for ventilation [1]. Optimum levels of indoor humidity should be desired to be reached and maintained to ensure a comfortable and healthy environment. Desiccant cooling systems have advantages in environmentally friendly operation and separate control of sensible and latent cooling loads, which leads to comfortable indoor air quality. In addition, the desiccant cooling system is

a heat-driven cycle and therefore has the ability to use low-grade energy such as natural gas, waste heat and solar energy.

Desiccant cooling can be used either in a standalone system or a hybrid system coupled with a vapor compression refrigeration-based air-conditioning system or free energy such as solar or industrial waste heat [2]. In hybrid systems, more efficient cooling occurs over a wide range of operating conditions when a vapor compression refrigeration-based air-conditioning system is combined with a desiccant cooling system. This is because in a hybrid system, first the desiccant dehumidifier efficiently removes the moisture from the fresh ventilated air before it enters the conditioned space, and then, the vapor compression system removes only sensible heat from the conditioned space. This type of arrangement removes the requirement of a low dew point temperature of the evaporator cooling coil and subsequently reheating.

Numerous studies have assessed the feasibility of desiccant cooling systems using simulations and experimental methodologies to make them energy-efficient and cost-effective. The reported studies are related to feasibility studies [3–5] performance predictions [6, 7], wheel optimization [8–14] and development of new materials [15–18]

The wide spread use of this technology is not yet possible due to its relatively large size and low system performance. Mittal and Khan [19] evaluated the performance and energy-saving capacity of a desiccant cooling system composed of silica gel bed. Compared to conventional air conditioners where indoor air is completely recycled, the electricity saving is approximately 19%. Advanced desiccant materials and novel system configurations have significant potential to improve performance and reliability. Therefore, improving performance can play a key role in economic feasibility. Further improvements in the energy utilization rate, reductions in cost and size, competitive design and production are the key issues faced by solid desiccant cooling techniques for obtaining more extensive acceptability in the field of space cooling.

The wheel, where an air-to-air heat and mass transfer takes place at a low rotation speed, is the most crucial component of the desiccant cooling system. Therefore, mathematical modeling of the desiccant wheel plays an important role in enhancing the overall system performance. The optimum wheel speed and thickness, and the operating parameters such as the air flow rate, the relative humidity of the inlet air and the regeneration air temperature on the wheel performance have all been examined [11–13, 20–23]. The relationship between the regeneration temperature and the area ratio of the process and regeneration parts has been examined [12]. Most of the studies have investigated balanced flow, i.e., the wheel is split equally between the process and regeneration air flows. It is commonly accepted that as the regeneration temperature decreases, the regeneration section becomes a larger portion of the wheel. According to the manufacturer's catalog, a 1:3 split is generally used at high regeneration temperatures and a 1:1 split is used for low regeneration temperatures. However, it is doubtful that each area ratio effectively covers such a broad temperature range.

The adsorbent properties are also closely linked to enhanced performance. The development of advanced desiccant materials is focused on improving the sorption capacity, the moisture and heat diffusion rates, and the equilibrium isotherms [24]. In addition to the sorption capacity and favorable isotherms, a system performance of these new adsorbents need to be evaluated [17, 18].

From the viewpoint of system performance, the contribution and optimum condition of each component in the desiccant system, such as the regenerative evaporative cooler (REC) and sensible heat exchanger, need to be examined in detail. In addition to the contribution of each system component, the contributions of operating conditions such as outdoor conditions, regenerative temperature and rate of outdoor influx also need to be examined.

Researchers have also developed different cycles to achieve high system performance [9, 13, 25–27]. For each configuration, the evaluation of the contribution of each system component is required to find the optimal configuration.

Heat and mass transfer are coupled, and multiple parameters are involved in understanding the complicated phenomena in desiccant wheels. Mathematical models are commonly accepted as an effective method for analyzing the performance of the rotary wheels and systems. The models can also be used to guide system operation, interpret experimental results and assist in system design and optimization. In this work, a brief review on the mathematical modeling of the desiccant wheel is examined, and some typical issues and results of case studies are discussed.

## 2.2 Modeling

### 2.2.1 System Description

Jani et al. [2] made a comparison of various desiccant cooling cycles for air-conditioning and examined the influence of variations in outdoor conditions on the effectiveness of the system. Figure 2.1 shows a typical desiccant cooling system compared with a conventional air-conditioning system using vapor compression refrigeration. In the conventional system, air must be dehumidified by cooling it below its dew point to meet the latent load (② → ③), and reheating is often required (③ → ④) to satisfy the sensible heat factor (SHF). This implies very poor energy efficiency, particularly for low SHF, i.e., high latent cooling load. Additionally, a very low temperature can create a cold draft in the air-conditioned space.

In a solid desiccant cooling system, the moisture in the ventilated/recirculated process air is first removed using a rotating desiccant wheel. The temperature of this dried process air is then further lowered to the desired room conditions using of sensible heat exchangers and evaporative cooler. To make the system work continually, the amount of water vapor adsorbed by the rotating desiccant wheel must

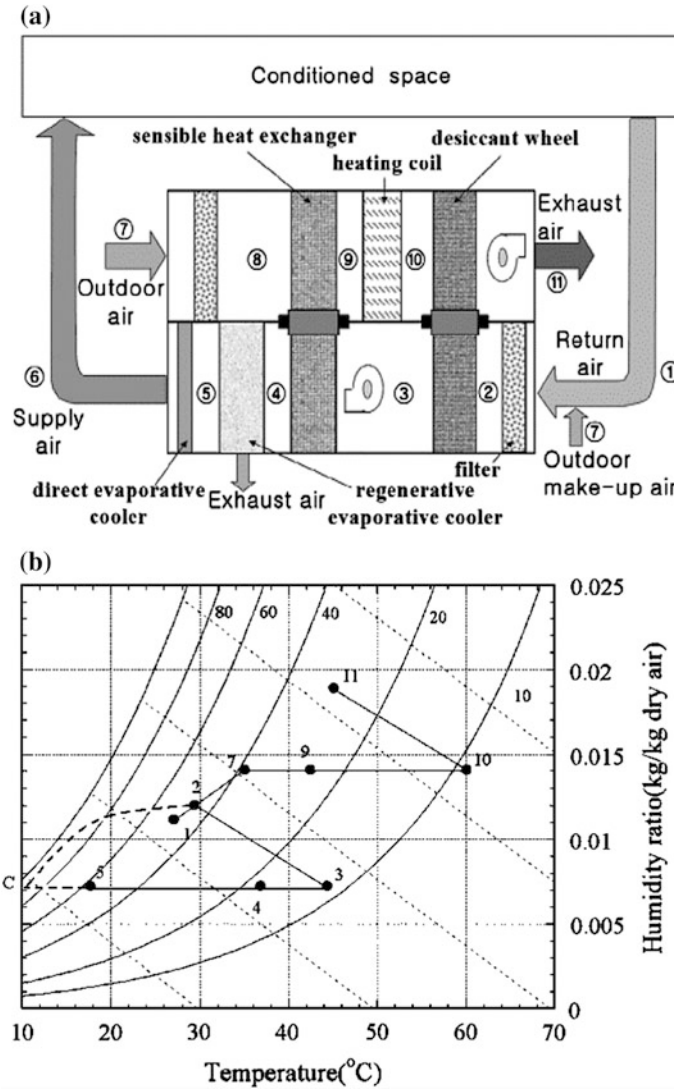


**Fig. 2.1** **a** Schematic of a desiccant cooling system and **b** corresponding psychrometric processes compared with a conventional air-conditioning system using vapor compression refrigeration [13]

be removed from the desiccant material so that it can be sufficiently dried, i.e., regenerated to adsorb the water vapor in the next cycle. This is achieved using a rotating cylindrical wheel divided into two sections: the adsorption section and the regeneration section. The desiccant material is heated to regeneration temperature, which is dependent upon the material, i.e., the desiccant used. The energy required for regeneration of the rotary desiccant wheel is supplied through the regeneration heat source, which is either an electrical heater or solar/waste heat.

It is more helpful to understand the physics by expressing the process in the psychrometric chart. The heated and dehumidified supply air exits from the humidification section of the wheel (②  $\rightarrow$  ③). The processed air operates close to an enthalpic process; therefore, the outlet temperature of the processed air will be very high, which reduces the sorption capacity of the desiccant. A sensible heat exchanger (③  $\rightarrow$  ④) and an evaporative cooler (④  $\rightarrow$  ⑤) are required to cool the dried processed air before it is introduced into occupied spaces. The sensible heat exchanger acts as a pre-cooler after the desiccant and also as a preheater before the regeneration section, which results in enhanced performance of the whole system.

Regeneration occurs on the other side of the partition where the heated air enters, usually from the opposite direction, and then passes over the desiccant and finally exhausts from the dehumidifier (⑩  $\rightarrow$  ⑪). The ideal outlets of process and regeneration are the points of intersection between lines of constant relative humidity and enthalpy passing through the inlets of process (②) and regeneration (⑩), respectively.

### 2.2.2 *Mathematical Modeling*

The advantages of mathematical models are that it takes less time and cost than experimental methods to predict the performance of a desiccant wheel. Therefore, mathematical models are very convenient to perform parametric research and optimization analysis. In addition, they can predict fundamental physics and surface chemistry of rotary desiccant wheels. Consequently, constructing valid mathematical models for desiccant wheels has become a key subject of many studies.

Mathematical modeling of desiccant wheels is a difficult task because the heat and mass transfer are coupled and too complicated to completely understand. Several mathematical models have been constructed and employed to analyze, develop and design desiccant wheels. Ge et al. [28] reviewed the literature on mathematical models and classified the models according to the modeling types of the heat and mass transfer between the humid air in the air channel and the desiccant wall. The models can be classified into two main categories: (1) gas-side resistance (GSR) model and (2) gas and solid-side resistance (GSSR) model. In the GSR model, heat and mass transfer within the solid desiccant are not taken into account. The governing equations have relatively simple forms with lower accuracy. The GSSR model can be further subdivided into the pseudo-gas-side (PGS) model, the gas and solid-side (GSS) model and the parabolic concentration profile (PCP) model.

GSSR models are higher in precision and more complex compared with GSR models. However, the PGS model requires extensive experimental data to determine the lumped transfer coefficients with different desiccant materials, and its reliability is not good enough. The GSS model also suffers from greater computational effort than the PGS model because of the additional second-order heat and

mass transfer diffusional items. The PCP model also has limitations including the assumption that a parabolic concentration profile for moist concentration exists at all the times in the desiccant particle.

The two-dimensional GSS model was expressed by Charoensupaya and Worek [29].

Conservation of moisture in the process air is expressed as:

$$\frac{\dot{m}_a}{X_m} \left( \frac{1}{u} \frac{\partial Y_a}{\partial t} + \frac{\partial Y_a}{\partial z} \right) = 2K_y(Y_d - Y_a) \quad (2.1)$$

Conservation of moisture in the desiccant felt is denoted as:

$$\varepsilon_t \rho_{ad} \frac{\partial Y_d}{\partial t} + (1 - \varepsilon_t) \rho_d \frac{\partial W}{\partial t} - D_G \rho_{ad} \frac{\partial^2 Y_d}{\partial r^2} - D_S \rho_d \frac{\partial^2 W}{\partial r^2} = 0 \quad (2.2)$$

where  $D_G$  and  $D_S$  represent the effective gas phase diffusivity and surface diffusivity, respectively.

Conservation of energy within the desiccant felt is represented with the following equation:

$$\varepsilon_t \rho_{ad} \frac{\partial H_{ad}}{\partial t} + (1 - \varepsilon_t) \rho_d c_{pd} \frac{\partial T_d}{\partial t} - k_d \frac{\partial^2 T_d}{\partial r^2} = (1 - \varepsilon_t) \rho_d H_{sor} \frac{\partial W}{\partial t} \quad (2.3)$$

where the subscript ad represents the air in the desiccant pore.

The rate of energy transfer between the process air and desiccant felt can be expressed as:

$$\frac{\partial H_g}{\partial t} + u \frac{\partial H_g}{\partial z} = \frac{2K_y}{\rho_a \alpha_a} (Y_d(t, x, \alpha_d) - Y_a) \frac{\partial H_g}{\partial Y_a} + \frac{2h}{\rho_a \alpha_a} (T_d(t, x, \alpha_d) - T_a) \quad (2.4)$$

To save computation time, it is desired to take into account the smallest dimension as possible in the model. Because the variation in moisture and temperature is more significant in the axial direction, it is often chosen as main direction for heat and mass transfer when constructing the governing equations. Sphaier and Worek [30] compared one-dimensional and two-dimensional mathematical models for both the solid-side and gas-side resistance and found that the one-dimensional formulation could be used in desiccant wheel applications, whereas a two-dimensional model was needed for an enthalpy wheel when thermal resistance in the desiccant material was high.

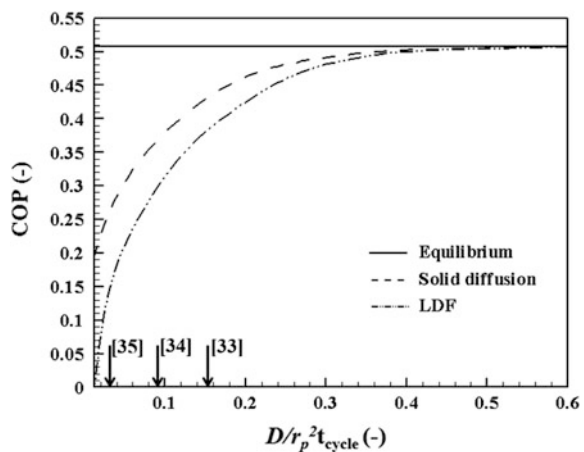
Mass transfer kinetics of adsorbent particles from the inter-particle or intra-particle viewpoint is an interesting issue in adsorption physics. The inter-particle mass transfer models include isobaric and non-isobaric models. The isobaric models are over-simplified to completely ignore the inter-particle resistance. Ahn et al. [31] reported that isobaric models are only valid in certain restricted ranges.



Intra-particle mass transfer models include equilibrium, linear driving force (LDF) and solid diffusion models. Solid diffusion models reflect the physical essence of mass transfer in the intra-particle resistance. However, they are complex and difficult to solve; therefore, their application is limited. Therefore, in many cases, simplified models, such as the LDF model or the equilibrium model, are used. The LDF model assumes the uptake profile within the particle as a parabolic function, and the equilibrium model assumes the uptake as a constant. However, there are few discussions on the application range of these simplified intra-particle models even for the equilibrium model, which is obviously incorrect considering that the required equilibrium time is approximately 300 min, which is much longer than a typical cycle time. Hong et al. [32] discussed the validity of the simplified intra-particle models of equilibrium and LDF by comparing them to the solid diffusion model.

Figure 2.2 shows the behavior of the coefficient of performance (COP) according to the non-dimensional diffusion ratio,  $t_{\text{cycle}}D/r_p^2$  for each different intra-particle diffusion model. For the entire range of non-dimensional diffusion ratios, the equilibrium model overestimates the performance of the adsorption bed and plays a role in the upper limit of performance. In contrast, the LDF model, which is the most commonly used model to analyze the intra-particle mass transfer kinetics, underestimates the performance of the adsorption bed. The differences between the models become smaller as the non-dimensional diffusion ratio increases. Therefore, the equilibrium model and the LDF model can be used if the non-dimensional diffusion ratio is over a critical value, for example 0.312 for the equilibrium model and 0.228 for the LDF model, with less than 5% relative error from the solid diffusion model. Some other cases of the RD-type silica gel that is frequently used in previous studies [33–35] are provided with their respective non-dimensional diffusion ratios in Fig. 2.2. Note how much the equilibrium and the LDF models distort the performance of the adsorption refrigerator system. The

**Fig. 2.2** Comparison of the COP of the three different models according to the non-dimensional diffusion ratio [32]



three cases of the typical RD-type silica gel used in the earlier studies [33–35] are overestimated for the equilibrium model by 94.2, 35.0 and 17.7%, respectively, and the earlier studies are underestimated for the LDF model by 45.0, 20.9 and 11.4%, respectively. Therefore, the intra-particle diffusion model should be carefully implemented to avoid seriously distorted results that may occur without serious consideration of the non-dimensional diffusion ratio of the adsorbent.

### 2.2.3 Chanel Geometrics

Desiccant wheels consist of a frame with a thin layer of desiccant material. The channels of the desiccant wheel frame are fabricated in various structures such as honeycomb, triangular, sinusoidal [36]. Studies have been conducted, mostly on one-dimensional analysis of channel section [37, 38]. However, there has been scanty research interest on channel shape or channel section area. Al-Sharqawi and Lior [39] and Chung et al. [40] introduced a comparative numerical solution of a heat and mass transfer problem in ducts with different cross-sectional geometries such as circular, square and triangular.

Figure 2.3 illustrates the typical channel shapes. Previous studies have identified the hydraulic diameter and Nusselt number for each channel shape. For example, the hydraulic diameter and Nusselt number for a sine-shaped channel (Fig. 2.3) are shown in Eqs. (2.5)–(2.8). The Lewis number for the mass transfer was set at 1 in all cases.

$$D_h/b = (1.0542 - 0.4670\alpha^* - 0.1180\alpha^{*2} + 0.1794\alpha^{*3} - 0.043\alpha^{*4}) \cdot \alpha^* \quad (2.5)$$

$$Nu_T = 1.1791 \times (1 + 2.7701\alpha^* - 3.1901\alpha^{*2} - 1.9975\alpha^{*3} - 0.4966\alpha^{*4}) \quad (2.6)$$

$$Nu_H = 1.903 \times (1 + 0.4556\alpha^* + 1.2111\alpha^{*2} - 1.6805\alpha^{*3} + 0.7724\alpha^{*4} - 0.1228\alpha^{*5}) \quad (2.7)$$

$$Nu = (Nu_T + Nu_H)/2 \quad (2.8)$$

where  $\alpha^* = a/b$ , and  $a$ ,  $b$  are the channel height and width, respectively.

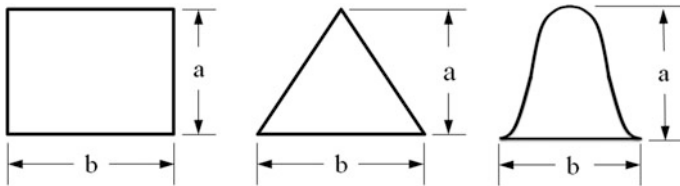


**Fig. 2.3** Channel shapes considered in this study

**Fig. 2.4** Variation in the heat transfer coefficient according to the channel shape and size [40]

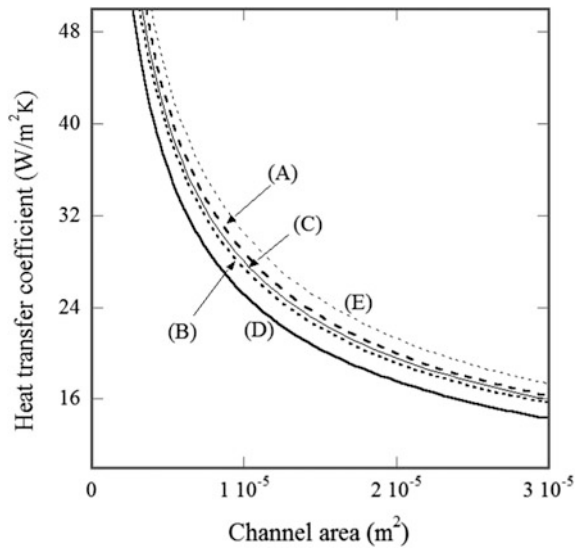
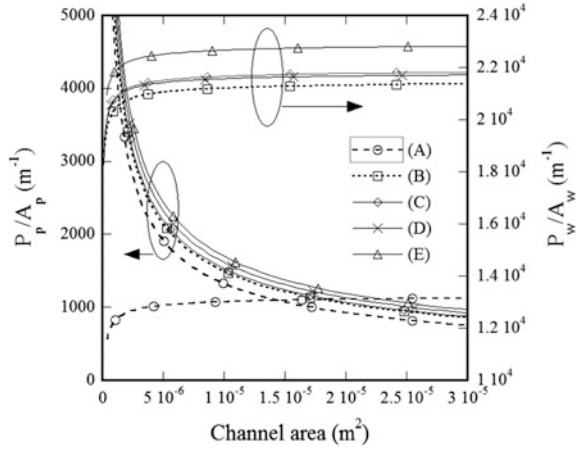


Figure 2.4 shows changes in heat transfer according to the channel shape and section area. (A) indicates a rectangular channel, (B) a triangular channel, (C) a sine-shaped channel ( $a:b = 1:1$ ), (D) a sine-shaped channel ( $a:b = 1:2$ ), and (E) a sine-shaped channel ( $a:b = 2:1$ ). The amount of heat transfer was compared for the desiccant wheel with same channel section area but different channel shape. A triangular channel and a sine-shaped channel have a similar hydraulic diameter and Nusselt number. Conversely, a rectangular channel has a greater hydraulic diameter and Nusselt number and as a result has a larger heat/mass transfer for the same section area. Therefore, a rectangular channel may be more efficient than a triangular or sine-shaped channel. However, the performance of a desiccant wheel cannot be solely judged by the Nusselt number. As Fig. 2.5 shows, the circumference of the unit channel area and the unit desiccant area can also influence the performance of a desiccant wheel. A greater unit-area circumference results in more efficient heat/mass transfer, which explains why a triangular or sine-shaped channel is more efficient than a rectangular channel. [39], who did not included a sine-shaped channel in their study, have also showed that triangular ducts provide higher convective heat and mass transfer and absorb 11 and 42% more water than square and circular ducts, respectively. Gao et al. [37] discussed the effect of the felt thickness and the passage shape on the performance of a desiccant wheel and found that as the thickness of the sorbent increases, the moisture removal capacity (MRC) of the desiccant wheel improves, and a sinusoidal air flow passage was the best shape for greater MRC.

For the same sine-shaped channel, the amount of heat transfer may vary greatly according to the aspect ratio. In the case of (E), the amount of heat transfer was greatest at an aspect ratio of  $a:b = 2:1$ .

**Fig. 2.5** Circumference of the unit channel area and unit desiccant area [40]



**Fig. 2.6** Effect of channel shape on the performance of the desiccant wheel [40]

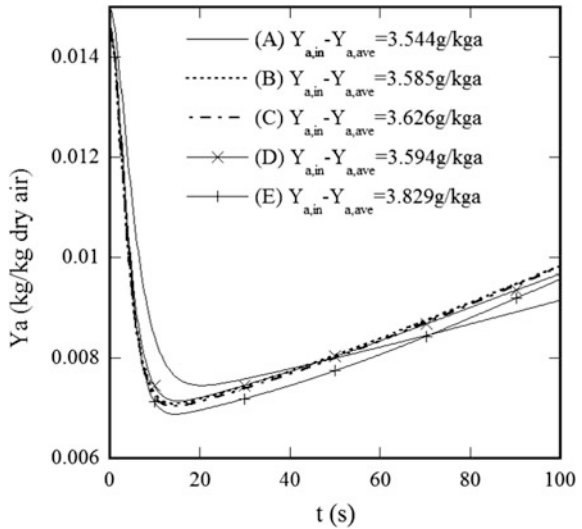


Figure 2.6 shows the influence of the channel shape corresponding to Fig. 2.4 for the same channel section area. It presents average humidity ( $Y_a$ ) at the outlet of the dehumidification section according to time. The index of performance, which is the amount of dehumidification or the difference between the humidity at the inlet and the average humidity at the outlet of the dehumidification section ( $Y_{a,in} - Y_{a,ave}$ ), is also included.

To compare the influence of each factor, two additional sets of data were examined and compared to the standard condition: air flow rate,  $u_a = 2.0$  m/s; channel section area =  $1 \times 10^{-5}$  m<sup>2</sup>; channel wall thickness,  $c = 0.15 \times 10^{-3}$  m; channel length,  $L = 0.3$  m; mass fraction of the desiccant,  $f_m = 0.7$ ; desiccant

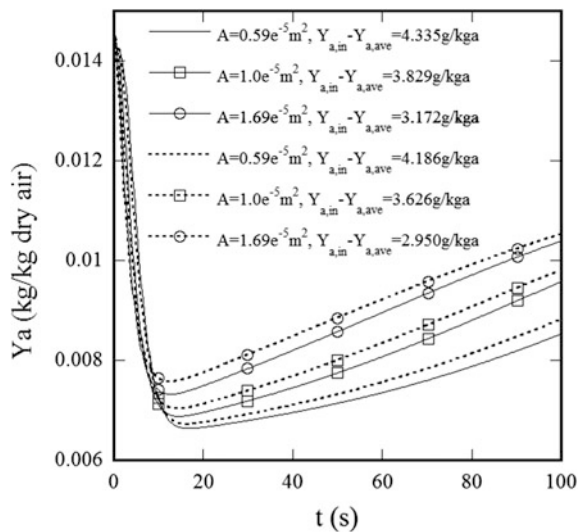
separate factor,  $R = 0.1$ ; maximum water uptake capacity,  $W_{\max} = 0.4$ ; dehumidification time,  $t_p = 100$  s; and the area ratio of regeneration to the dehumidification section,  $t_r/t_p = 0.8$ . The silica gel properties were used for  $\rho, c_p$ .

A sine-shaped channel with an aspect ratio  $a:b = 2:1$  showed the best excellent dehumidification performance and had the highest heat transfer (Fig. 2.4) and greatest circumference (Fig. 2.5). The most widely used sine-shaped channel with an aspect ratio  $a:b = 1:1$  did not show particularly superb performance compared to the other channel shapes. Specific data are not presented here, but the same trend was observed for different regeneration times (or rotating speed; 50 and 150 s) and an area ratio of 0.9 between the regeneration and the dehumidification section.

The channel section area was set at  $0.59 \times 10^{-5} \text{ m}^2$ ,  $1 \times 10^{-5} \text{ m}^2$  and  $1.69 \times 10^{-5} \text{ m}^2$  for a widely used sine-shaped channel (dotted line) and a sine-shaped channel with an aspect ratio  $a:b = 2:1$  (solid line), respectively, to measure the humidity distribution and amount of dehumidification at a desiccant wheel outlet (Fig. 2.7). Regardless of the channel shape, both had better performance with a smaller channel section area. For the latter, the amount of dehumidification increased 13.2% when the section area diminished by  $1.3^2$  times compared to the standard condition ( $1 \times 10^{-5} \text{ m}^2$ ). The improvement was much greater than the sine-shaped channel with an aspect ratio  $a:b = 1:1$ , which had only a 5.3% increase. The consequent pressure decline does not have a significant impact on the overall cooling system. To improve the performance of a desiccant wheel, it is important to diminish the channel section area.

Variations in wheel size were examined for the mass fraction ( $f_m = 0.7/1.3, 0.7, 0.7 \times 1.3, 0.7 \times 1.5$ ), specific heat ( $c_p/1.5, c_p/1.3, c_p, 1.3c_p$ ), density ( $\rho/1.3, \rho, 1.3\rho, 1.5\rho$ ) and isothermal curve ( $R = 0.05, 0.1, 0.4, 1.0$ ). By

**Fig. 2.7** Effect of the channel size on the performance of a desiccant wheel [40]



adjusting the channel shape and section area, the channel length  $L$  could be reduced by 43% to yield the same performance under standard conditions. By improving the properties of the desiccant, the size of a desiccant wheel could be reduced by 29%, while maintaining the same dehumidification capacity. When the channel factors and desiccant factors were combined under optimal conditions (sine-shaped channel with an aspect ratio 2:1, channel area  $0.59 \times 10^{-5} \text{ m}^2$ , desiccant mass  $1.3f_m$ , specific heat  $c_p/1.3$ , density  $1.3\rho$  and  $R = 0.4$ ), the size of a desiccant wheel could be reduced by as much as 66% to perform on the same level as under standard conditions (sine-shaped channel with an aspect ratio 1:1, channel area  $1 \times 10^{-5} \text{ m}^2$ , desiccant mass  $0.7f_m$ , specific heat  $c_p$ , density  $\rho$  and  $R = 0.1$ ). The results of the analysis also suggest that the channel section area is the most influential factor that decides the size of a wheel, followed by the separate factor  $R$  and the channel shape.

### 2.2.4 Adsorbent

At present, commercially available desiccants include silica gel, activated alumina, natural and synthetic zeolites, titanium silicate, lithium chloride and synthetic polymers. Silica gel is one of the best performing and commonly investigated materials in desiccant wheels owing to its good long-term stability, minimal hysteresis and availability of data in the literature for comparison and specification. However, it is not a heat-resistant material and therefore is only adequate for low regeneration temperatures.

Zeolites are a common alternative to silica gel because they have widespread chemical uses and can be synthesized according to the application requirements. Conventional zeolites, such as Type A and Type Y, show a typical S-shaped adsorption isotherm, which is ideally suited for dehumidification and drying processes. However, their adsorption isotherm generally has a zone of steepest gradient in the low humidity range, i.e., the minimal amount of adsorbed water vapor is achieved only at extremely low relative humidity. A new generation of zeolites has raised interest both in adsorbent characterization and cooling applications. AQSOA™ (Aqua Sorb Adsorbent) zeolites, recently developed by Mitsubishi Plastics Inc., is an interesting solution to exploit low-grade heat. With this new generation of zeolites, a favorable S-shaped isotherm remains and the steepest gradient zone of the adsorption isotherm is shifted toward higher relative humidity values compared with conventional zeolites such as Type A or Type Y [41]. The experimental results of several studies are available on alternative desiccant materials [42]; however, only a few have investigated the new generation of zeolites [17], and neither a comprehensive nor a model-driven numerical analysis has been carried out on AQSOA zeolite-based desiccant wheels.

The apparently favorable moisture adsorption characteristics of AQSOA are alleged to improve the dehumidification performance of the wheel. However, recent

experimental results [17] showed that silica gel performed as well and sometimes better than the alternative materials over a range of conditions comparing desiccant wheels using silica gel, a super adsorbent polymer and a ferroaluminophosphate (FAM-Z01) zeolite material. It was not clear whether these performance differences were attributed to differences in the desiccant adsorption isotherms or to other material properties. Recently, Hong et al. [18] discussed this issue.

Silica gel has a linear-shaped isotherm, which causes a slow adsorption rate and small adsorption capacity; however, it has some attractive characteristics such as a lower adsorption heat ( $\sim 2400$  kJ/kg) than zeolites, which reduces the amount of input energy required to remove the heat from the exothermic reactions. FAM-Z01 has a high adsorption rate and a large adsorption capacity due to its S-shaped isotherm, which increases the possibility of it becoming commercially available. Kim et al. [43] developed a hybrid isotherm equation combining both the Henry and Sips equations, from which a comparison of adsorption rates was made between FAM-Z01 and various conventional silica gels (Type-A5BW, Type-RD 2560 and Type-A++). They showed that FAM-Z01 has a larger adsorption capacity than silica gels. The characteristics of FAM-Z01, particularly its isotherm, have been investigated. However, although the isotherm is important to the adsorption capacity, it is only one factor among various parameters that have a complex effect on the system performance. By individually examining the effect of each parameter, the guidelines for developing a new adsorbent can be obtained.

$$q^* = \beta K_H \left( \frac{P}{P_s} \right) + (1 - \beta) \frac{q_m \left( K_S \frac{P}{P_s} \right)^{1/n}}{1 + \left( K_S \frac{P}{P_s} \right)^{1/n}} \quad (2.9)$$

Equation (2.9) is a combined isotherm equation of both the Henry and Sips equations for FAM-Z01, which was proposed by Kim et al. [43]. The valid range of Eq. (2.9) is  $20^\circ\text{C} < T_b < 80^\circ\text{C}$ . The total of nine coefficients that appeared in Eq. (2.9) was obtained using the following equations:

$$K = K_0 \exp \left( -\frac{H_{\text{sor}}}{R_v T_b} \right) \quad (2.10)$$

$$n = A + \frac{B}{T} \quad (2.11)$$

$$\beta = \exp \left( -\alpha \frac{P}{P_s} \right) \quad (2.12)$$

$$\alpha = \kappa_1 + \kappa_2 \frac{T}{T_{\text{ref}}} \quad (2.13)$$

**Table 2.1** Coefficients used in the FAM-Z01 isotherm equation [18]

Coefficient	Value	Coefficient	Value
$K_{0,H}$	$4.717 \times 10^{-3}$	$H_{\text{sor},H}$	$-8.773$
$\kappa_1$	9.097	$\kappa_2$	$-3.569$
$K_{0,S}$	$6.288 \times 10^{-2}$	$H_{\text{sor},S}$	$-11.24$
$A$	$-7.734 \times 10^{-1}$	$B$	$2.732 \times 10^2$
$q_m$	$2.175 \times 10^{-1}$	$R^2$	0.989

The coefficients used in Eq. (2.9)–(2.13) are shown in Table 2.1. The isotherm equations of the conventional silica gels in the form of the Freundlich or Toth equation are as follows:

Type-RD silica gel [44]

$$q^* = A(T_b) \left( \frac{P}{P_s} \right)^{B(T_b)} \quad (2.14)$$

The simulation results for FAM-Z01 and Type-RD silica gel applied to the fin-tube-type adsorption bed in  $0.09 < P/P_s < 0.40$  are shown in Fig. 2.8 and Table 2.2. Kim et al. [43] ascertained that the performance of the adsorption bed is directly proportional to the adsorption rate, but Fig. 2.8a shows that the adsorption chill using FAM-Z01 has only a 2.1% higher  $\Delta q_{\text{max}}$ . The COP of the FAM-Z01/water systems is 14.4% lower and 3.87% higher than that of the Type-RD silica gel, respectively.

The performance of the FAM-Z01/water system is expected to be enhanced because of the increased adsorption capacity due to the nature of the S-shaped isotherm. However, the results show a decreased COP compared to the Type-RD silica gel/water system for the same conditions ( $0.09 < P/P_s < 0.40$ ). To examine the cause of the low performance of FAM-Z01, we artificially changed the thermo-physical properties of Type-RD silica gel to match FAM-Z01, one by one,

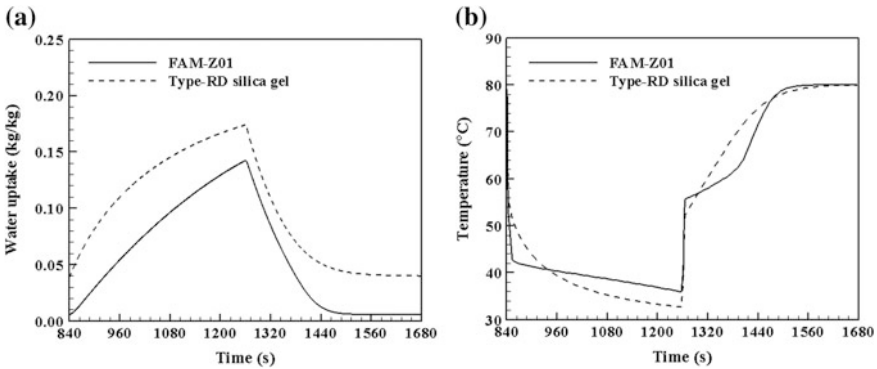


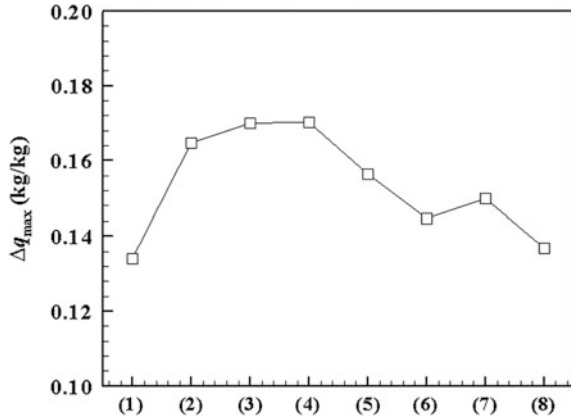
**Fig. 2.8** Comparison of the **a** volume-averaged water uptake and **b** volume-averaged bed temperature between FAM-Z01 and Type-RD silica gel [18]



**Table 2.2** Performance of each adsorption bed with the FAM-Z01/water and Type-RD silica gel/water systems [18]

	FAM-Z01	Type-RD silica gel
$\Delta q_{\max}$ (kg/kg)	0.1368	0.1340
COP	0.5623	0.6572

**Fig. 2.9** Variation of the  $\Delta q_{\max}$  after changing the thermo-physical properties, 2 isotherm, 3 density, 4 specific heat, 5 adsorption heat, 6 thermal conductivity and 7 porosity from 1 Type-RD silica gel to 8 FAM-Z01 [18]



and examined the  $\Delta q_{\max}$  and COP. Case (1) on the x-axis in Fig. 2.9 corresponds to Type-RD silica gel. Case (2) represents changing the isotherm property to match FAM-Z01, while keeping the remaining properties of Type-RD silica gel the same. Case (3) represents changing the isotherm and density to match FAM-Z02, while keeping the remaining properties of Type-RD silica gel the same. In the same manner, FAM-Z01's (4) specific heat, (5) adsorption heat, (6) thermal conductivity, (7) porosity and (8) diffusion coefficient were substituted in consecutive order. Finally, case (8) is the result of FAM-Z01. Although case (2)–case (7) are artificial, this strategy provides insight about which property of FAM-Z01 increases or decreases the system performance and the influence each property has on the system performance.

Figure 2.9 and Table 2.3 show the variation of  $\Delta q_{\max}$ , according to the changes in the thermo-physical properties one by one, from Type-RD to FAM-Z01. The bigger the  $\Delta q_{\max}$ , the larger the cooling energy  $Q_{\text{eva}}$ . Case (2), where the isotherm of FAM-Z01 was used, has a 22.9% higher  $\Delta q_{\max}$  than Case (1), i.e., Type-RD silica gel. This advantage originates from FAM-Z01's S-shaped isotherm. Case (3), where the density of FAM-Z01 was additionally used, has a 3.28% higher  $\Delta q_{\max}$  than case (2). The density of FAM-Z01 is lower than Type-RD silica gel. When the density is changed to a low value, the heat transfer capacity is increased; therefore, the mass transfer resistance is reduced. The increased mass transfer capacity causes the adsorption bed to reach the pressure of the evaporator or condenser more rapidly. As a result, the  $\Delta q_{\max}$  is increased. Case (4) is the results obtained by the

**Table 2.3** Rate of increase in system performance [18]

	$\Delta q_{\max}$ (%)	COP (%)
Case (1)	0	0
Case (2)	+22.9	+4.47
Case (3)	+3.28	-0.58
Case (4)	+0.06	-0.64
Case (5)	-8.11	-16.1
Case (6)	-7.54	-1.00
Case (7)	+3.67	+0.63
Case (8)	-8.74	-0.93

addition of the specific heat of FAM-Z01. The specific heat of FAM-Z01 is lower than the Type-RD silica gel, which results in a lower thermal resistance. The  $\Delta q_{\max}$  is increased by the enhanced heat transfer capacity. However, the effect of the specific heat is minor (only a 0.06% increase). The adsorption heat of FAM-Z01 was added to case (5). The adsorption heat indicates the degree of the exothermic and endothermic reactions coming from the phase change in the adsorbate. The larger the adsorption heat, the stronger the reaction, which increases the thermal resistance of the adsorption bed. FAM-Z01 has a 30% larger value of adsorption heat than Type-RD silica gel, which results in an 8.11% decrease in the  $\Delta q_{\max}$ . Case (6), with the addition of the thermal conductivity of FAM-Z01, shows a 7.54% lower  $\Delta q_{\max}$  than case (5). Thermal conductivity is also proportional to the heat transfer capacity. The lower thermal conductivity of FAM-Z01 decreases  $\Delta q_{\max}$ . The porosity of FAM-Z01 was added to case (7). Adsorption occurs by diffusion on the pore surface of the adsorbent (particle); therefore, the adsorption rate is enhanced by large porosity. However, the proportion of vapor with low thermal conductivity is also increased when the porosity is large, which reduces the effective thermal conductivity. The simulation result indicates that the lower porosity of FAM-Z01 increases the  $\Delta q_{\max}$  by 3.67%. Case (8) is the case where the diffusion coefficient of FAM-Z01 ( $D_{so}/\exp(-E_a/(R_u T_b))$ ) is added, and finally all the properties of FAM-Z01 are used. The adsorption rate is enhanced as the  $D_{so}$  increases and the  $E_a$  decreases. Li et al. [45] showed that the diffusion coefficient of FAM-Z01 is lower than Type-RD silica gel. The smaller diffusion coefficient enlarges the intra-particle mass transfer resistance and decreases the  $\Delta q_{\max}$  by 8.74%.

In conclusion, the adsorption rate is increased by the S-shaped isotherm, small density, small adsorption heat, large thermal conductivity, small porosity and large diffusion coefficient. Conversely, the characteristics of FAM-Z01, such as large adsorption heat, low thermal conductivity and low diffusion coefficient, are the factors that decrease the adsorption rate.

### 2.2.5 Isotherm

Inside the porous medium, two phases of water (vapor and adsorbed water) coexist in an equilibrium state, which is characterized by the water vapor–adsorbent sorption isotherm. There are many types of equilibrium adsorption relationships. The relative humidity of the moist air in equilibrium with the adsorbent,  $\phi$ , and the separation factor,  $R$ , is used to calculate the water content of the adsorbent,  $W$ :

$$W/W_{\max} = \phi/[R + (1 - R)\phi] \quad (2.15)$$

Some researchers consider that  $W$  is a function of  $\phi$  and the temperature of the moist air in equilibrium with the adsorbent  $T_d$  can be represented as:

$$W = f(T_d, Y_d) = g(T_d, \phi) \quad (2.16)$$

Sometimes it is assumed that  $W$  is a function of  $\phi$  only, and invariable with the temperature  $T_d$ :

$$W = f(\phi) \quad (2.17)$$

In the previous section, we showed that the performance of a desiccant wheel depends on the properties of the adsorbent, but the most influential factor was the isotherm. For the development of a new adsorbent, the isotherm would be one of the targets to find the optimal isotherm shape that leads to maximum dehumidification and explains the reason why the isotherm shape enhances dehumidification on a particular working condition.

From the viewpoint of the regeneration temperature, when the regeneration temperature increases, the wheel operates at a lower mean relative humidity. Therefore, the ideal isotherm is shifted so that the maximum possible moisture gradient occurs over the encountered range of relative humidity. However, it is hard to draw a general conclusion because the ideal isotherm shape varies according to the supply and regeneration air inlet conditions.

In previous studies, a different optimal isotherm shape was reported in each study. Collier et al. [46] found that a general moderately convex isotherm shape gives the best compromise between efficient dehumidification and regeneration processes. However, Zheng et al. [10] found that an isotherm with  $R = 0.07$  resulted in the maximum dehumidification performance for Type 1. Dai et al. [11] presented that the desiccant isotherm shape is the most important factor in determining the wave front shapes within the desiccant matrix. They also discussed the effect of the separation factor ( $R = 0.01$ – $1$ ) of the isotherm shape on the regeneration temperature of the desiccant wheel.

### 2.2.6 Analytic Modeling

Analytic modeling is very important to provide physical insight and a basis for the examination of numerical and experimental results. However, analytic approaches are subject to extensive assumptions; therefore, they cannot explain the complex phenomena involved in coupled heat and mass transfer in desiccant wheels. Most of the previous studies are based on numerical models and analytical studies are scarce. Banks [47, 48] assumed that a desiccant wheel might be represented by the superposition of two heat transfer regenerators driven by combined potentials and presented methods for predicting exit air-conditions. However, intense numerical computation is eventually required due to the nonlinear nature involved in the solutions, which restricts the practical applicability of analytical methods to engineering practices. Lee et al. [49] and Kim et al. [50] presented analytical solutions for the simplified governing equations based on assumption of linear temperature and concentration profiles [49] and uniform heat and mass fluxes [50] at the air-desiccant interface.

Recently, Lee and Kim [51] proposed a simple, yet accurate, integral model and validated the model by comparing with a FDM model and experimental data in the literature. The analysis of the solution revealed that the behavior of a desiccant wheel depends primarily on three dimensionless numbers of the thermal time constant and the Jakob numbers, namely  $C_r^*$ ,  $Ja_a$  and  $Ja_s$ . The dimensionless numbers ( $Ja_a$  and  $Ja_s$ ) are the thermodynamic characteristics of an air-desiccant system that decide the behavior of a desiccant wheel.

### 2.2.7 Numerical Modeling

Numerical simulation of heat and moisture interactions between the air stream and the particles in a desiccant bed provides useful insight into the dynamics of the bed and its performance characteristics. Assessing the great number of available options and their optimum combinations involved in the design of a desiccant wheel is a time-intensive task when using an experimental approach. Therefore, modeling and numerical simulations are highly effective tools when designing a desiccant wheel because they effectively isolate one variable at a time to examine trends and causes. Different methods of numerical solution have been used by many researchers with different simplified treatments of the fluid and solid domains to predict the behavior of air dehumidifying systems [28].

Figure 2.10 shows the schematic of a desiccant wheel. A desiccant wheel is made by either impregnating a honeycomb-patterned microstructure wheel with a solid desiccant (e.g., silica gel or zeolite), or by coating the same substance on corrugated sheet and rolling it into a wheel. A desiccant rotor contains numerous channels, with a fixed ratio of the regeneration to the dehumidification section. A desiccant section absorbs water, and a slow-revolving desiccant wheel moves the

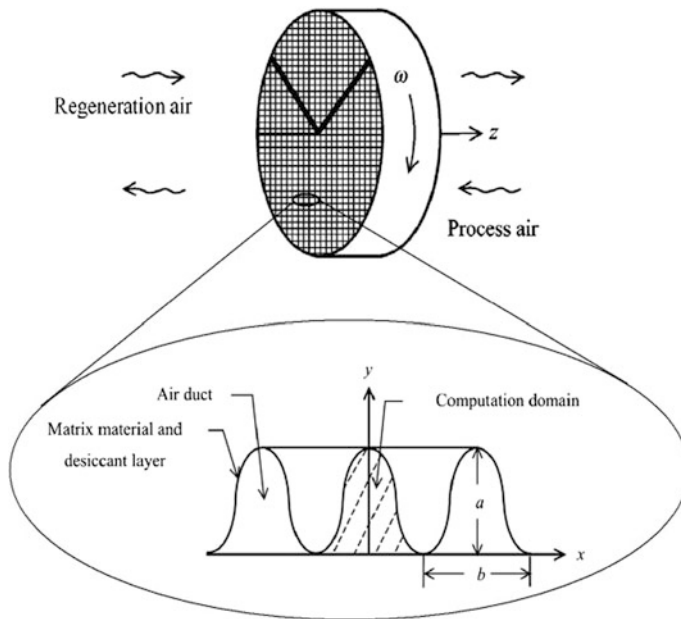


**Fig. 2.10** Schematic of a desiccant wheel and the computational domains [22]

section to the high-temperature regeneration section to restore the dehumidifying ability. Then, the desiccant part returns to its initial stage.

Multi-dimensional mathematical models reflecting the effects in radial or circumferential directions can be used to analyze the heat and mass transfer processes comprehensively with improved accuracy. However, the complexity increases simultaneously. Most physical models used in numerical studies of desiccant wheels have been analyzed through 1-D mathematical formulations based on the hypotheses of negligible cross-direction resistance to heat and mass transfer inside the desiccant wall [11, 12, 22, 37, 52–54]. The validity of one-dimensional models is acceptable to relatively thin desiccant walls of the hygroscopic matrix and has been investigated in some studies [30, 55, 56].

Because of the geometric similarity and to avoid prohibitive computation costs, it is reasonable to represent the multiple annular layers of straight slots in the desiccant wheel using a “representative annulus” whose cross-sectional view is presented in Fig. 2.10. In this way, the three cylindrical coordinates ( $r, \theta, z$ ) can reasonably be reduced to a steady two-dimensional ( $\theta, z$ ) or unsteady one-dimensional ( $t, z$ ) problem. In the present study, the unsteady one-dimensional model ( $t, z$ ) is chosen for the coupled heat and mass transfer process in the rotary desiccant wheel. The numerical analysis is based on the following assumptions:

- (1) The airflow is one-dimensional;
- (2) The axial heat conduction and mass diffusion in the fluid are neglected;

- (3) There is no leakage of fluid in the desiccant wheel;
- (4) All ducts are impermeable and adiabatic;
- (5) The thermodynamic properties are constant and uniform; and
- (6) The heat and mass transfer coefficient between the airflow and the desiccant wall is constant along the channel.

### 2.2.7.1 Governing Equations

Based on the above assumptions, the energy and mass conservation equations can be obtained as follows [20, 57].

Mass conservation for the process air:

$$\frac{\partial Y_a}{\partial z} = \frac{h_m P_p}{u_a \rho_a A_p} (Y_d - Y_a) \quad (2.18)$$

where the left-hand and right-hand sides represent the sorbate influx by the fluid flow and the sorbate transfer rate to the felt, respectively. Contrary to the adsorbent, the moisture storage in the air can be neglected.

Energy conservation for the process air:

$$(C_{pa} + Y_a C_{pv}) \frac{\partial T_a}{\partial z} = \frac{h P_p}{u_a \rho_a A_p} (T_d - T_a) \quad (2.19)$$

where the left-hand side represents the sum of the energy transferred by the fluid flow and decreased by the sorbate transfer to the felt, and the right-hand side represents the conduction heat transfer to the felt. Again, the energy storage in the humid air can be neglected.

Conservation of water content for the absorbent:

$$\frac{\partial W}{\partial t} = \frac{h_m P_d}{\rho_d f_m A_d} (Y_a - Y_d) \quad (2.20)$$

where the left-hand and right-hand sides represent the moisture storage term inside the desiccant and the convective mass transfer between the air and the desiccant, respectively. A mass diffusion within the solid desiccant in the axial direction is neglected.

Conservation of energy for the absorbent:

$$(C_{pd} + f_m W C_{pl}) \frac{\partial T_a}{\partial t} = \frac{h P_d}{\rho_d A_d} (T_a - T_d) + \frac{h_m H_{sor} P_d}{\rho_d A_d} (Y_a - Y_d) \quad (2.21)$$

where the first term on the left-hand side is the energy transfer by heat conduction and the second term is energy transfer by mass transfer. The first term on the

right-hand side of Eq. (2.21) calculates the convective heat transfer between the solid desiccant and air. The second term on the right-hand side expresses the influence of the adsorption heat.

### 2.2.7.2 Boundary and Initial Conditions

The above equations are subject to the following boundary and initial conditions, which are easily obtained considering the periodic nature of the desiccant wheel.

For the process section:

$$T_{ap}(t, 0) = T_{ap,in} \quad (2.22a)$$

$$Y_{ap}(t, 0) = Y_{ap,in} \quad (2.22b)$$

$$T_{dp}(0, z) = T_{dr}(t_r, L - z) \quad (2.22c)$$

$$Y_{dp}(0, z) = Y_{dr}(t_r, L - z) \quad (2.22d)$$

For the regeneration section:

$$T_{ar}(t, 0) = T_{ar,in} \quad (2.23a)$$

$$Y_{ar}(t, 0) = Y_{ar,in} \quad (2.23b)$$

$$T_{dr}(0, z) = T_{dp}(t_p, L - z) \quad (2.23c)$$

$$Y_{dr}(0, z) = Y_{dp}(t_p, L - z) \quad (2.23d)$$

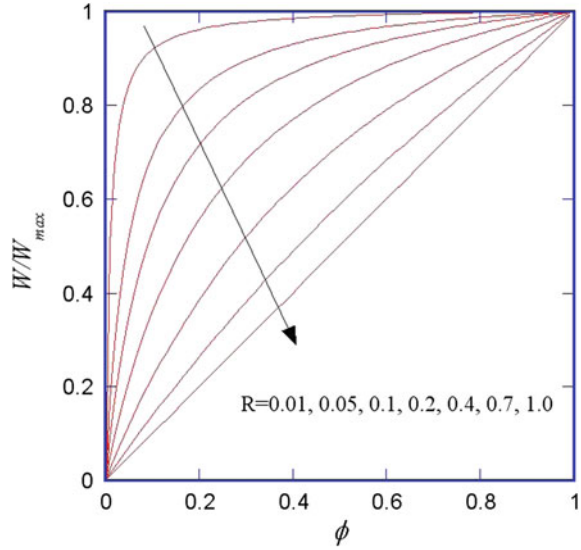
### 2.2.7.3 Auxiliary Equations

The governing Eqs. (2.18)–(2.21) have 5 unknowns  $T_a$ ,  $T_d$ ,  $Y_a$ ,  $Y_d$ , and  $W$ . To solve this set of equations, i.e., to close the problem, it is necessary to relate the equilibrium composition  $Y_d$  to the water content  $W$  and temperature of the adsorbent  $T_d$ . Here, we employ silica gel as the desiccant material; therefore, the water content in the desiccant is governed by the following isotherm [58, 59]:

$$\phi_d = 0.0078 - 0.0576 W + 24.2 W^2 - 124 W^3 + 204 W^4 \quad (2.24)$$

where  $\phi_d$  is the equilibrium relative humidity over the desiccant with a water content  $W$ .

**Fig. 2.11** Schematic of the isotherm shape according to the separate factor



Here, we employ another isotherm as follows:

$$\frac{W}{W_{\max}} = \frac{\phi_d}{R + (1 - R)\phi_d} \quad (2.25)$$

where  $\phi_d$  is the equilibrium relative humidity over the desiccant with a water content  $W$  and  $R$  is the separate factor. Figure 2.11 shows the adsorption capacity behavior according to the separate factor. It is obvious to expect a larger adsorption capacity (i.e., a higher wheel performance) for a higher  $W_{\max}$ . Therefore, we fixed  $W_{\max} = 0.4$  and confined our attention to the effect of  $R$  on the optimal operation conditions.

The relationship between the humidity ratio and the relative humidity is expressed as:

$$Y_d = \frac{0.622\phi_d P_s}{P - \phi_d P} \quad (2.26)$$

In addition, the values of the adsorption heat  $H_{\text{sor}}$ , convective transfer coefficient  $h$ , thermal conductivity  $k$  and moisture diffusivity  $D_e$  in the desiccant material are required.

Typical diffusion theory holds that the water vapor molecule has three types of diffusion modes in porous mediums: Fickian diffusion, Knudsen diffusion and surface diffusion. Fickian diffusion and Knudsen diffusion occur in series in the pore, and these two diffusions are summarized as the pore diffusion. Moreover, the pore diffusion and the surface diffusion occur in parallel. Fickian diffusion occurs when the mean free path is relatively short compared to the pore size. Knudsen



diffusion is dominant when the mean free path of gas molecules is relatively long compared to the pore size. Pesaran and Mills [60] reported that surface diffusion is a dominant one in moisture transfer in micro-porous silica gel (regular density silica gel). However, for macro-porous silica gel (intermediate density silica gel), both Knudsen diffusion and surface diffusion are important mechanisms. Fickian diffusion can be negligible for silica gel at atmospheric pressure.

The effective diffusivity associated with Knudsen diffusion in a porous desiccant medium can be written as [61]:

$$D_{K,eff} = 97r_v \sqrt{\frac{T + 273.15}{R_v} \frac{\varepsilon_v}{\tau_v}} \quad (2.27)$$

The effective diffusivity associated with the surface diffusion of adsorbed water  $D_{s,eff}$  in a porous desiccant medium is directly influenced by the path tortuosity  $\tau$  and depends on the adsorbate–adsorbent pair. In the present work, the following equation was used [61]:

$$D_{s,eff} = \frac{D_{s0}}{\tau_1} \exp\left(\frac{-4.5 \times 10^{-4} H_{sor}}{bR_v(T + 273.15)}\right) \quad (2.28)$$

where  $b$  depends on the type of adsorption bond and  $D_{s0}$  is a constant that depends on the adsorbent.

#### 2.2.7.4 Numerical Procedures

The aforementioned governing equations are discretized into finite difference equations by an implicit, forward difference scheme. All the simulations in this paper are performed with a grid of 800 for time and 50 for space. The grid independence has been proved to be valid within a tolerable limit. A cyclic steady state is obtained within 10 iterations with a relative error of  $1 \times 10^{-5}$  which is a root mean square of  $\Delta\phi = |(\phi - \phi^{old})/\phi|$ ,  $\phi = T_a, T_d, Y_a, Y_d$ . The relative error of the uptake mass with the release mass is lower than 0.5%.

Simulations have been conducted for a desiccant wheel with a width of 0.2 m and a silica gel wall thickness of 0.15 mm. The geometry of the channels in the wheel shown in Fig. 2.10 is sinusoidal with a width ( $b$ ) of 3.5 mm and a height ( $a$ ) of 1.75 mm. The air velocity is 2 m/s in both the adsorption and regeneration period. The convective heat transfer coefficient and hydraulic diameter are expressed in Eqs. (2.5)–(2.8) from the Nusselt number in the sinusoidal-shaped channels [62]. Table 2.4 includes the data for all the properties and geometries employed in the simulations.

**Table 2.4** Input data used in the simulations

Channel shape	Sinusoidal
Height, $a$	$1.75 \times 10^{-3}$ m
Width, $b$	$3.5 \times 10^{-3}$ m
Wall thickness, $c$	$0.15 \times 10^{-3}$ m
Wheel length	0.2 m
Facing area	1 m <sup>2</sup>
Facing air velocity, $u_a$	2.0 m s <sup>-1</sup>
Desiccant material	
Mass fraction of sorbent, $f_m$	0.7
Capacity, $C_{pd}$	921 J kg <sup>-1</sup> K <sup>-1</sup>
Density, $\rho_d$	720 kg m <sup>-3</sup>
Heat of sorption, $H_{sor}$	$2502.68 + C_{pv}T_a$ kJ kg <sup>-1</sup>
Air density, $\rho_a$	1.1614 kg m <sup>-3</sup>
Capacity, $C_{pa}$	1007 J kg <sup>-1</sup> K <sup>-1</sup>
Thermal conductivity, $k_a$	0.0263 W m <sup>-1</sup> K <sup>-1</sup>
Water vapor capacity, $C_{pv}$	1872 J kg <sup>-1</sup> K <sup>-1</sup>
Liquid capacity, $C_{pl}$	4186 J kg <sup>-1</sup> K <sup>-1</sup>

### 2.2.8 Performance Index

The main function of a desiccant wheel is to remove the water vapor from the process air. Therefore, the performance indices represent the dehumidification capacity of the desiccant dehumidifier. There are several performance indices such as moisture removal, relative moisture relative efficiency, effectiveness of the wheel and the dehumidification coefficient of the performance of the wheel.

The primary performance indicator is assessed using the moisture removal capacity (MRC), as described in the ASHRAE proposed national standard method of testing [63]. The MRC quantifies the amount of moisture removed from the processing stream as it passes through the desiccant wheel using the following equation:

$$\text{MRC} = \dot{m}_p (Y_{\text{ap,in}} - Y_{\text{ap,out}}) \quad (2.29)$$

If the humidity is fixed at the process and regeneration inlets, the behavior of the MRC is usually similar to the effectiveness defined in Eq. (2.30), which is used in other literature [21, 57]. Based on the effectiveness, the best performance is obtained at the lowest adsorption-side outlet humidity,  $Y_{\text{ap,out}}$ .

$$\varepsilon_d = \frac{Y_{\text{ap,in}} - Y_{\text{ap,out}}}{Y_{\text{ap,in}}} \quad (2.30)$$

In the case of an unbalanced flow, the mass flow rate  $\dot{m}_p$  will change according to the ratio of the area of regeneration to dehumidification,  $A_r/A_p$ . Therefore, the MRC is more appropriate than  $\varepsilon_d$  as a performance index of unbalanced flow. At the optimum rotational speed, the MRC reaches a maximum; however, this does not mean a minimum value of  $Y_{ap,out}$  because the mass of the moisture removed can become larger not only by decreasing the outlet humidity of the process section, but also by increasing the area of the process section.

## 2.3 Research Issues and Case Studies

### 2.3.1 Wheel Speed

The desiccant wheel is the key component of a desiccant cooling system, and the optimum rotation speed is one of the most important factors that can improve the performance of the wheel. The rotation speed should not only be low enough for complete regeneration, but also be high enough to keep the adsorbent far from equilibrium. This conflict yields the optimum rotation speed. The existence of an optimum rotation speed, at which the humidity of the product air becomes minimized, has already been reported [20, 21].

#### 2.3.1.1 Dependence on the Regeneration Temperature and $A_r/A_p$

For outdoor conditions when  $T_{p,in} = 30^\circ\text{C}$  and  $\phi_{p,in} = 40\%$ , Fig. 2.12 shows the variation of the adsorption-side outlet humidity for various wheel speeds

**Fig. 2.12** Variations of adsorption-side outlet humidity for various wheel speeds at each regeneration temperature (60, 90, 120 and  $150^\circ\text{C}$ ) [12]

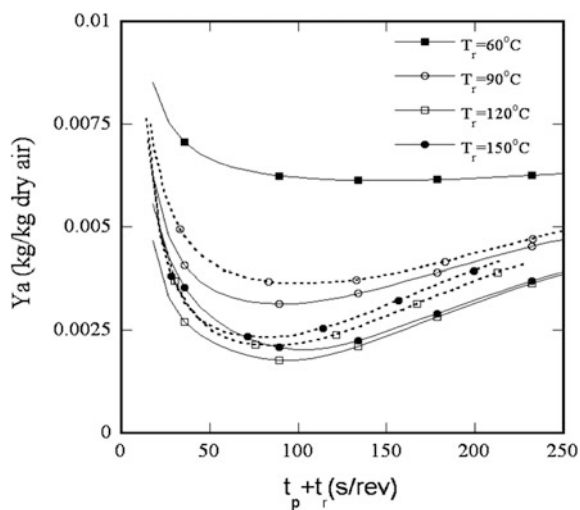
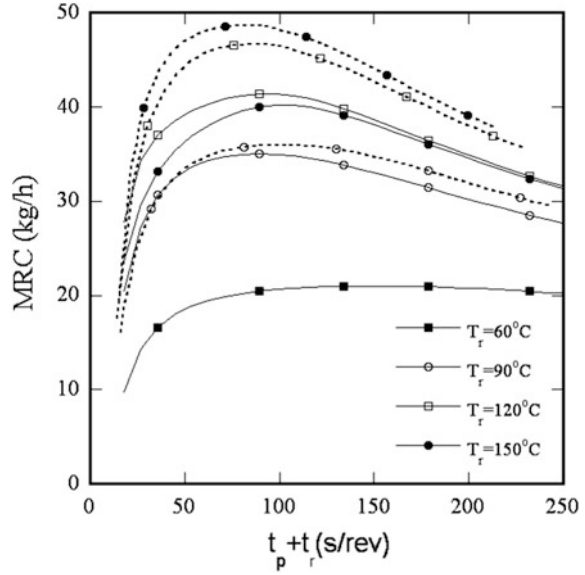


**Fig. 2.13** Variations of the MRC for various wheel speeds at each regeneration temperature (60, 90, 120 and 150 °C) [12]

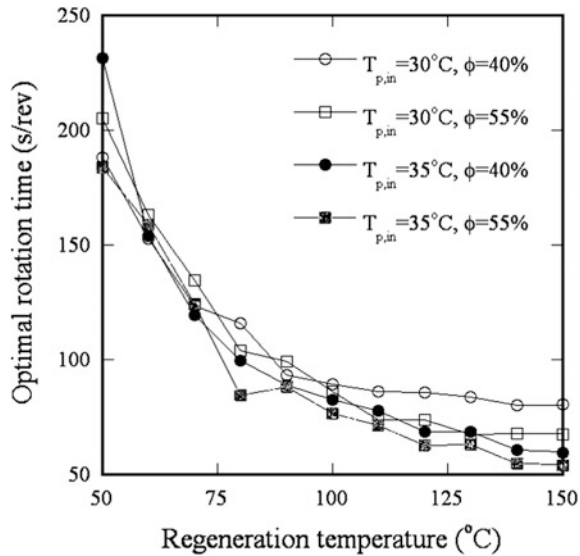


( $=3600/(t_p + t_r)$  rpm) for each regeneration temperature (60, 90, 120 and 150 °C). The optimum area ratio of process to regeneration,  $A_r/A_p$ , varies depending on the regeneration temperature, and the resulting optimum  $A_r/A_p$  is 0.784, 0.623, 0.521 and 0.424 corresponding to the regeneration temperatures 60, 90, 120 and 150 °C, respectively. The solid lines in Fig. 2.12 show the results for  $A_r/A_p = 0.784$ , and the dashed lines are for  $A_r/A_p = 0.784, 0.623, 0.521$  and 0.424. Note that the optimum value of  $A_r/A_p$  is obtained by maximizing the MRC. If the wheel diameter is fixed, the mass of the moisture removed can be increased not only by decreasing the outlet humidity of the process section, but also by increasing the process section area. Therefore, we cannot say that the optimum performance is found at the minimum value of the outlet humidity of the process section if the value of  $A_r/A_p$  is the design parameter. Figure 2.13 clearly shows this. If the MRC is chosen as an indicator of wheel performance, the maximum mass of moisture removed is found at the optimum value of  $A_r/A_p$ , but in Fig. 2.12, the minimum humidity is found at other values of  $A_r/A_p$ .

### 2.3.1.2 Dependence on the Regeneration Temperature and Outdoor Conditions

The variation of optimum wheel speed as a function of the regeneration temperature and outdoor conditions is shown in Fig. 2.14. For convenience, four outdoor conditions are nominated. Regardless of the outdoor conditions, as the regeneration temperature increases, the optimum wheel speed decreases and then approaches a

**Fig. 2.14** Variations of the optimum wheel speed as a function of the regeneration temperature and outdoor conditions [12]

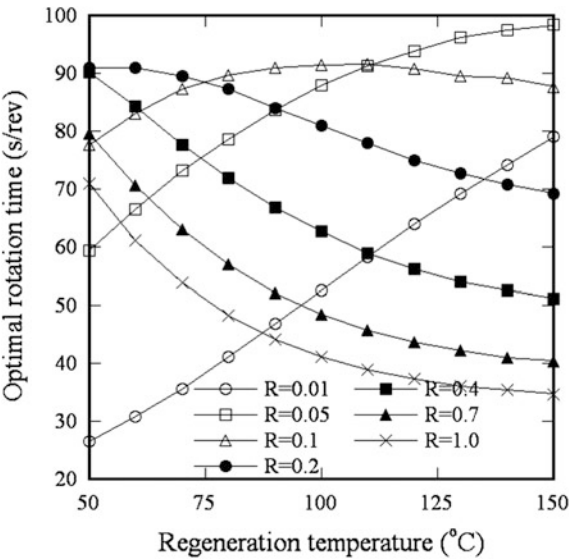


constant value. At low regeneration temperatures, the optimum speed is not as sensitive to the outdoor conditions compared with high regeneration temperatures. In addition, the optimum wheel speed is dependent on the outdoor humidity. The highest optimum wheel speed is observed for outdoor conditions  $T_{p,in} = 30^\circ\text{C}$  and  $\phi_{p,in} = 40\%$  where the humidity has the smallest value (10.6 g/kg). The optimum wheel speed is almost the same for the outdoor conditions  $T_{p,in} = 30^\circ\text{C}$ ,  $\phi_{p,in} = 55\%$  and  $T_{p,in} = 35^\circ\text{C}$ ,  $\phi_{p,in} = 40\%$ . Note that the humidity of these two outdoor conditions is very close (14.6 and 14.1, respectively). The humidity 19.6 g/kg, which corresponds to the outdoor conditions  $T_{p,in} = 35^\circ\text{C}$  and  $\phi_{p,in} = 40\%$ , results in the lowest optimum wheel speed. For the optimization procedure to maximize the MRC, the IMSL routine ZXMWd is linked to the program to evaluate the wheel performance.

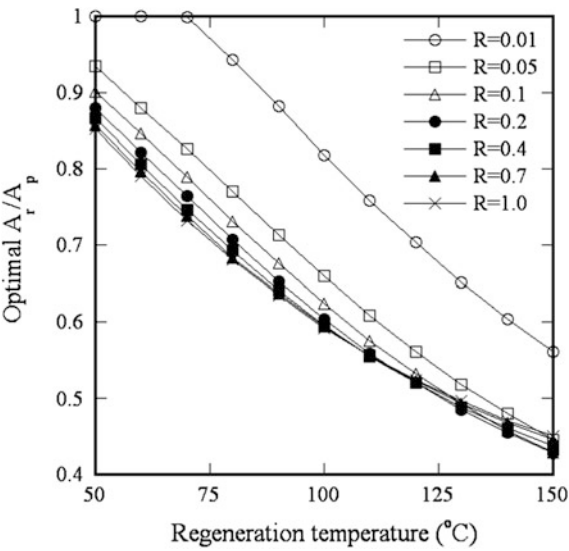
### 2.3.1.3 Dependence on the Isotherm

Figure 2.15 shows the optimal rotation speed and its dependency on the regeneration temperature and isotherm shape with different values for the separation factor  $R$  in Eq. (2.25). Note that the present results differ from earlier studies, which found that the optimum rotating speed was a condition of the fixed regeneration temperature and  $A_r/A_p$ . As the regeneration temperature increases, a monotonic decrease in the optimal rotation speed is observed  $R > 0.2$ , but the behavior is reversed as  $R$  becomes less than 0.2. Therefore, the highest optimum rotation speed is found at  $R = 0.2$  at low regeneration temperatures, but  $R = 0.05$  at high regeneration temperatures. The exceptional behavior of  $R = 0.01$  is explained by

**Fig. 2.15** Variations of the optimum rotation speed as a function of the regeneration temperature and isotherm shape [54]



**Fig. 2.16** Variations of the optimum value of  $A_r/A_p$  as a function of the regeneration temperature and isotherm shape [54]



observing differences in water content of process and regeneration. Note that at low regeneration temperatures, the optimum speed is not as sensitive to the isotherm shape compared with at high regeneration temperatures.

The effect of the value of  $A_r/A_p$  on the wheel performance is investigated at different regeneration temperatures and isotherm shapes. Variations in the optimum value of  $A_r/A_p$  as a function of the regeneration temperature are shown in Fig. 2.16 for each isotherm shape. The optimum value of  $A_r/A_p$  is more sensitive to the

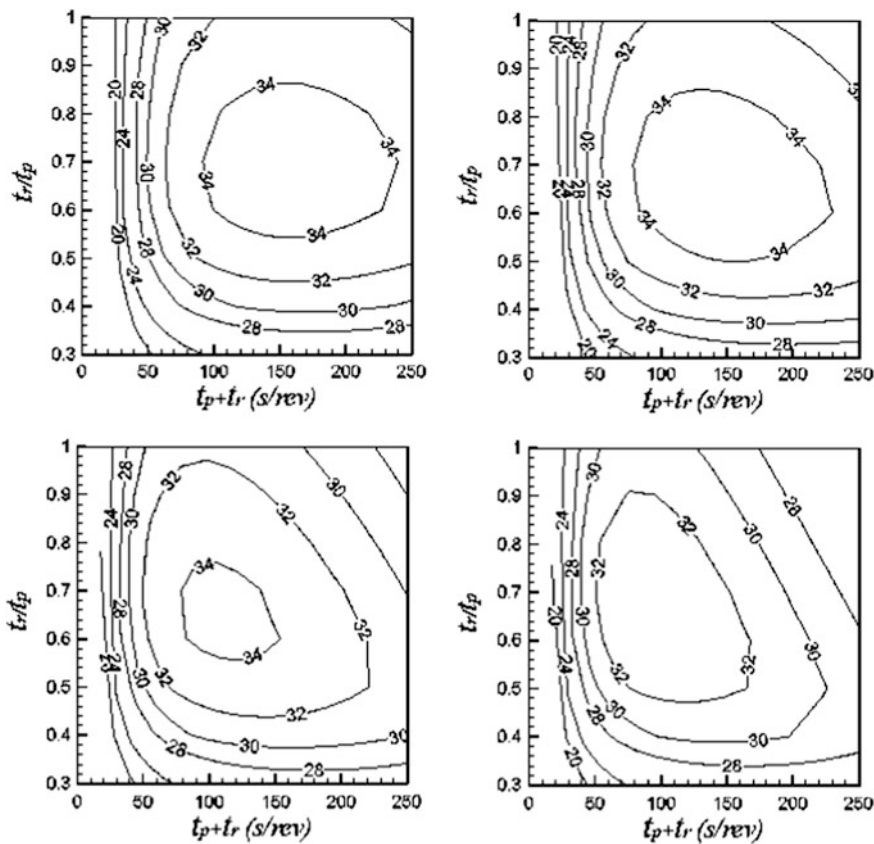


**Fig. 2.17** Profiles of the MRC as a function of the optimum rotation speed and  $A_r/A_p$  for the isotherm shapes ( $R = 0.05, 0.1, 0.4, 1.0$ ) and the regeneration temperature  $T_{ar,in} = 90^\circ\text{C}$  [54]

isotherm shape at low regeneration temperatures than at high regeneration temperatures. The detailed discussion on the dependency of the regeneration temperatures will be given in the following section.

Figure 2.17 shows the profile of the MRC as a function of the optimum rotation speed and  $A_r/A_p$  for isotherm shapes ( $R = 0.05, 0.1, 0.4$ , and  $1.0$ ) and the regeneration temperature  $T_{ar,in} = 90^\circ\text{C}$ . Note that in contrast to the present work, most of earlier works studied the optimum isotherm shape for a fixed regeneration temperature and  $A_r/A_p$ . As shown in Fig. 2.17, the optimal design parameters, here rotating speed and  $A_r/A_p$ , are different for each isotherm shape. This means if optimization is conducted on the condition of a fixed rotation speed and  $A_r/A_p$ , an incorrect optimum isotherm shape would be found. We expect this is why the earlier works found different optimum isotherm shapes.

The above discussions are based on outdoor conditions of  $T_{ap,in} = 30^\circ\text{C}$  and  $\phi_{ap,in} = 40\%$ , but general dependency on the isotherm shape is the same for other

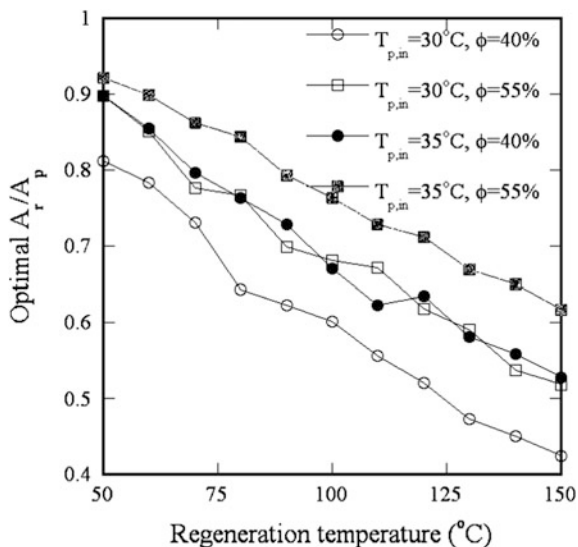
outdoor conditions such as  $T_{ap,in} = 35^\circ\text{C}$ ,  $\phi_{ap,in} = 40\%$  and  $T_{ap,in} = 30^\circ\text{C}$ ,  $\phi_{ap,in} = 55\%$  and  $T_{ap,in} = 35^\circ\text{C}$ ,  $\phi_{ap,in} = 55\%$ .

### 2.3.2 Area Ratio of Regeneration to the Dehumidification Section

As the regeneration temperature decreases, the regeneration section becomes a larger fraction of the wheel. According to the manufacturer's catalog, the 1:3 split is generally used for high regeneration temperatures and a 1:1 split for low regeneration temperatures. However, it is not easy to decide the optimal area ratio of regeneration/dehumidification, which is expected to vary according to not only the regeneration temperature, but also the desiccant isotherm and outdoor conditions. The dependence on the regeneration temperature and isotherm is already discussed in Sect. 2.3.1; therefore, we will focus on the dependence of the optimum value of  $A_r/A_p$  on the outdoor conditions for the adsorbent silica gel with the form of the isotherm in Eq. (2.24).

Variations of the optimum value of  $A_r/A_p$  as a function of the regeneration temperature are shown in Fig. 2.18 for four different outdoor conditions. We have determined the dependency of  $A_r/A_p$  on the outdoor humidity. As the humidity increases, the optimum value of  $A_r/A_p$  also increases. The results of Ahmed et al. [23] also show this dependency, but they did not provide any discussion of this issue. The lowest value of  $A_r/A_p$  is observed for the outdoor conditions  $T_{p,in} = 30^\circ\text{C}$  and  $\phi_{p,in} = 40\%$ , for which the humidity is 10.6 g/kg. The humidities for the

**Fig. 2.18** Variations of the optimum value of  $A_r/A_p$  as a function of the regeneration temperature and outdoor conditions [12]





outdoor conditions  $T_{p,in} = 30\text{ }^{\circ}\text{C}$ ,  $\phi_{p,in} = 55\%$  and  $T_{p,in} = 35\text{ }^{\circ}\text{C}$ ,  $\phi_{p,in} = 40\%$  are almost the same and show similar optimum values of  $A_r/A_p$  over the entire range of regeneration temperatures. The outdoor conditions with the highest humidity, i.e.,  $T_{p,in} = 35\text{ }^{\circ}\text{C}$ ,  $\phi_{p,in} = 40\%$  show the largest optimum value of  $A_r/A_p$ .

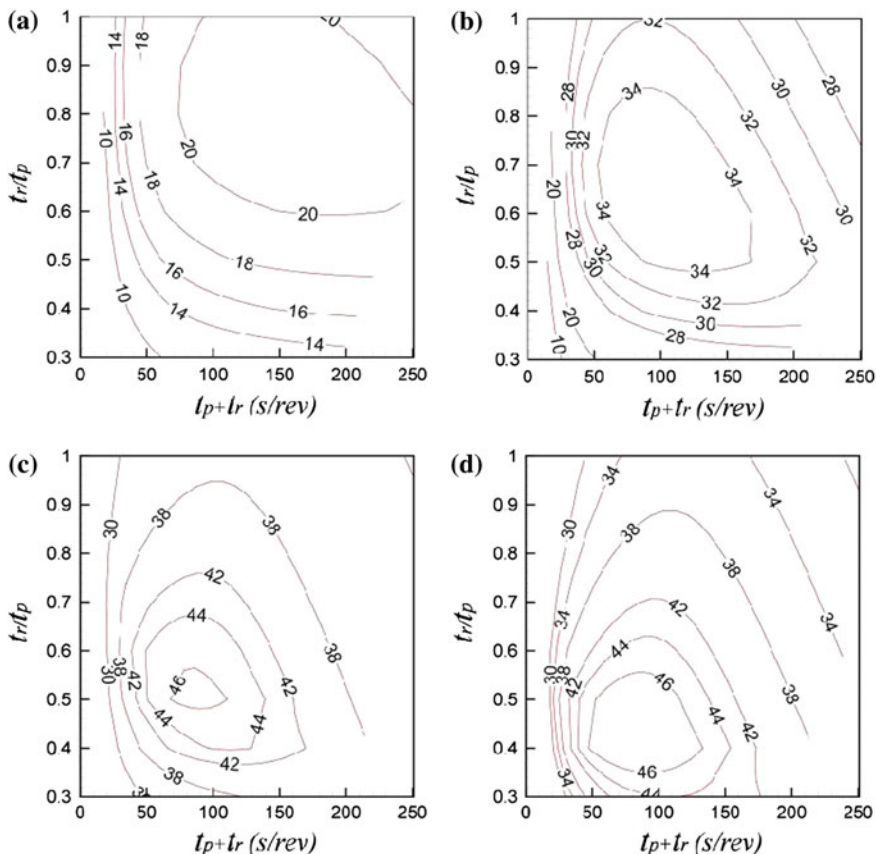
Ahmed et al. [23] ascertained that the optimum values of  $A_r/A_p$  are between 0.7 and 0.9 at  $T_{r,in} = 60\text{ }^{\circ}\text{C}$  and between 0.25 and 0.4 at  $T_{r,in} = 90\text{ }^{\circ}\text{C}$  depending on the inlet humidity. In Fig. 2.18, the optimum values of  $A_r/A_p$  are between 0.78 and 0.90 at  $T_{r,in} = 60\text{ }^{\circ}\text{C}$  for the inlet conditions studied, which is similar to the values reported by Ahmed et al. [23]. However, the optimum values of  $A_r/A_p$  are between 0.62 and 0.79 for  $T_{r,in} = 90\text{ }^{\circ}\text{C}$ , which shows considerable deviation from the values reported by Ahmed et al. [23]. The relationship between the optimum values of  $A_r/A_p$  and regeneration temperature is similar for a different isotherm shape as shown in Fig. 2.16 which covers a full range of isotherm shapes ( $0.01 < R < 1.0$ ).

Considering that  $A_r/A_p = 0.33$  is usually used for regeneration temperatures much higher than  $90\text{ }^{\circ}\text{C}$  and the regeneration section becomes a larger portion of the wheel as the regeneration temperature decreases, the results of Ahmed et al. [23] seem to under-predict the value of  $A_r/A_p$ . Note that in our study, the optimum value of  $A_r/A_p$  for  $T_{r,in} = 150\text{ }^{\circ}\text{C}$  is 0.42 for the outdoor conditions  $T_{p,in} = 30\text{ }^{\circ}\text{C}$  and  $\phi_{p,in} = 40\%$ , which is slightly greater than the value from the manufacturer's catalog (0.33).

Figures 2.19, 2.20, 2.21 and 2.22 show the profiles of the MRC as a function of the optimum wheel speed and  $A_r/A_p$  for the regeneration temperatures of 60, 90, 120 and  $150\text{ }^{\circ}\text{C}$  and four different outdoor conditions. The optimum behavior, i.e., the maximum MRC, wheel speed and optimum  $A_r/A_p$ , is discussed in previous sections, and here the behavior of off-design points is shown. With the sacrifice of a slight decrease in the MRC, the design point can be determined in the range of the wheel speed and  $A_r/A_p$ . We can also see that the desiccant wheel is highly effective for dehumidification at high regeneration temperatures [22].

### 2.3.3 Sensitivity to Outdoor Weather Conditions

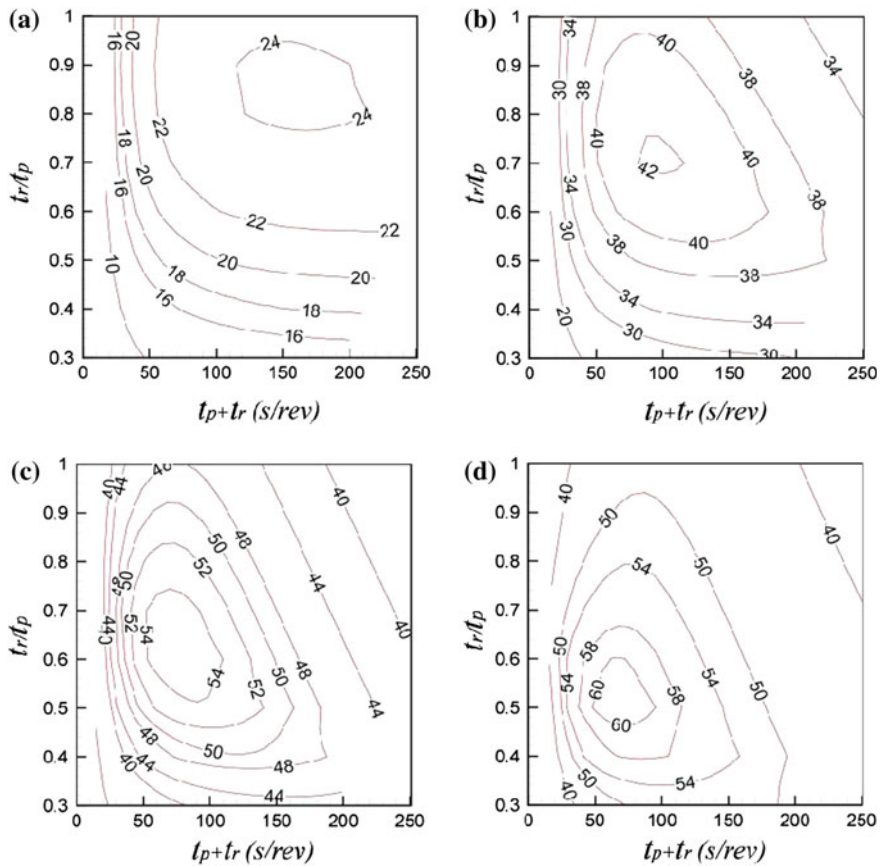
For the fixed area ratio  $A_r/A_p$ , Figs. 2.23, 2.24, 2.25 and 2.26 represent the effect of outdoor conditions ( $20\text{ }^{\circ}\text{C} < T < 35\text{ }^{\circ}\text{C}$ ,  $0.005 < Y < 0.025$ ) on the MRC for the regeneration temperatures of 60, 90, 120 and  $150\text{ }^{\circ}\text{C}$ . The performance decreases as the outdoor temperature increases or the outdoor humidity decreases. As the regeneration temperature increases, the effect of the outdoor temperature decreases. In particular, for low values of the outdoor humidity and high regeneration temperatures, the wheel performance is nearly independent of the outdoor temperature.



**Fig. 2.19** Profiles of the MRC as a function of the optimum wheel speed and  $A_r/A_p$  for the outdoor conditions  $T_{p,in} = 30\text{ °C}$  and  $\phi_{p,in} = 40\%$ ; **a**  $T_{r,in} = 60\text{ °C}$ , **b**  $T_{r,in} = 90\text{ °C}$ , **c**  $T_{r,in} = 120\text{ °C}$  and **d**  $T_{r,in} = 150\text{ °C}$  [12]

### 2.3.4 Isotherm

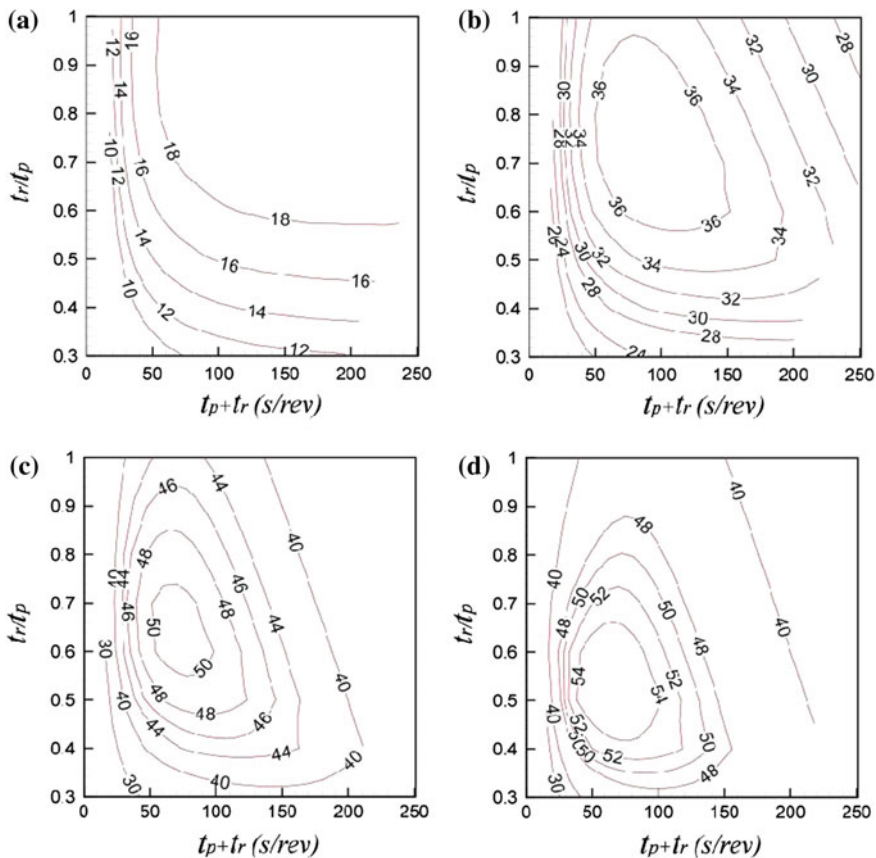
The separate factor  $R$  in Eq. (2.25) reflects the desiccant isotherm shape shown in Fig. 2.11. As  $R$  decreases, a larger adsorption capacity is expected even under low humidity. Dai et al. [6] suggested that  $R = 0.1$  for a low regeneration temperature ( $T_{ar,in} = 78.2\text{ °C}$ ), but should be  $R = 0.05$  for a high regeneration temperature ( $T_{ar,in} = 120\text{ °C}$ ). On the other hand, Simonson and Besant [64] ascertained that a linear sorption curve, i.e.,  $R = 1.0$ , has the highest effectiveness over a typical range of operation conditions. In our simulation, a higher MRC is expected as  $R$  decreases for the range of regeneration temperatures shown in Fig. 2.27. The only exception is  $R = 0.01$ . This can be explained by examining the water content difference evaluated by the process inlet ( $T_{ap,in} = 30\text{ °C}$  and  $\phi_{ap,in} = 40\%$ ) and the



**Fig. 2.20** Profiles of the MRC as a function of the optimum wheel speed and  $A_r/A_p$  for the outdoor conditions  $T_{p,in} = 30\text{ }^{\circ}\text{C}$  and  $\phi_{p,in} = 55\%$ ; **a**  $T_{r,in} = 60\text{ }^{\circ}\text{C}$ , **b**  $T_{r,in} = 90\text{ }^{\circ}\text{C}$ , **c**  $T_{r,in} = 120\text{ }^{\circ}\text{C}$  and **d**  $T_{r,in} = 150\text{ }^{\circ}\text{C}$  [12]

regeneration inlet ( $Y_{ar,in} = Y_{ap,in}$  and varying  $T_{ar,in}$ ) conditions. This value is closely related to the MRC.

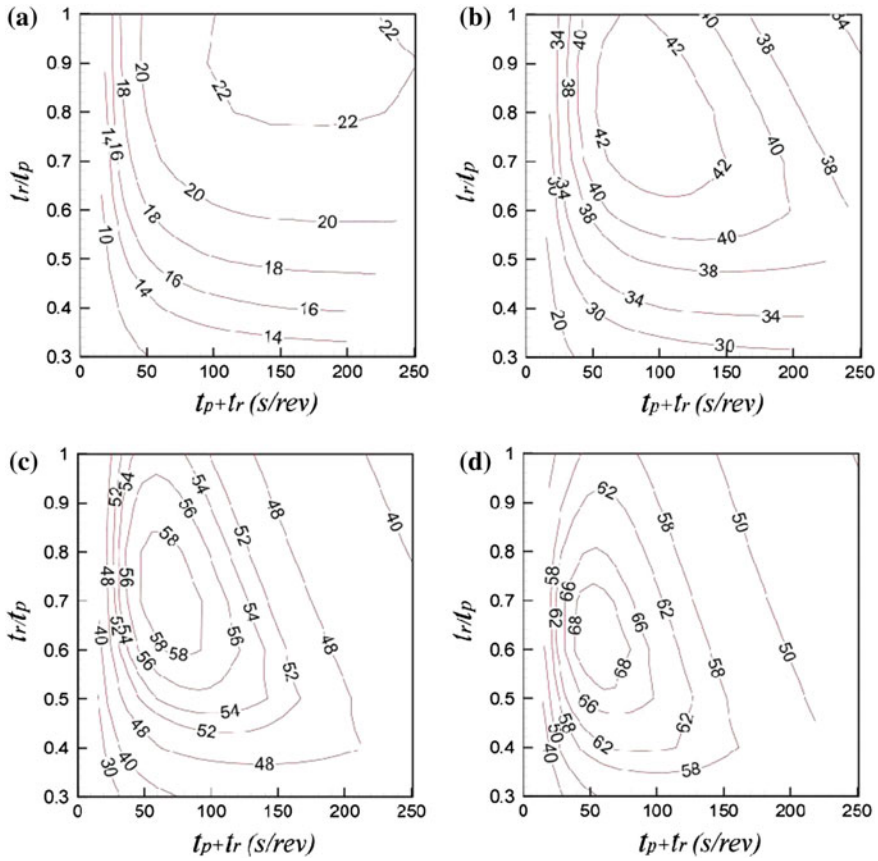
The large water content difference in the process and regeneration results has a large potential for moisture transfer, which increases the moisture removal capacity. Figure 2.28 shows a typical example. Figure 2.28a depicts the water content differences evaluated by the process inlet and regeneration inlet conditions of  $R = 0.05$  and  $R = 0.7$ , respectively, in the case of a low regeneration temperature. The water content difference is almost same at  $R = 0.7$  and  $R = 0.05$ . However, when the regeneration temperature is high, the relative humidity at the regeneration inlet decreases compared with low regeneration temperatures, and the water content difference is increased at  $R = 0.05$  than at  $R = 0.7$  as shown in Fig. 2.28b. Therefore, the isotherm shape of  $R = 0.05$  has a higher potential than that of



**Fig. 2.21** Profiles of the MRC as a function of the optimum wheel speed and  $A_r/A_p$  for the outdoor conditions  $T_{p,in} = 35$  °C and  $\phi_{p,in} = 40\%$ ; **a**  $T_{r,in} = 60$  °C, **b**  $T_{r,in} = 90$  °C, **c**  $T_{r,in} = 120$  °C and **d**  $T_{r,in} = 150$  °C [12]

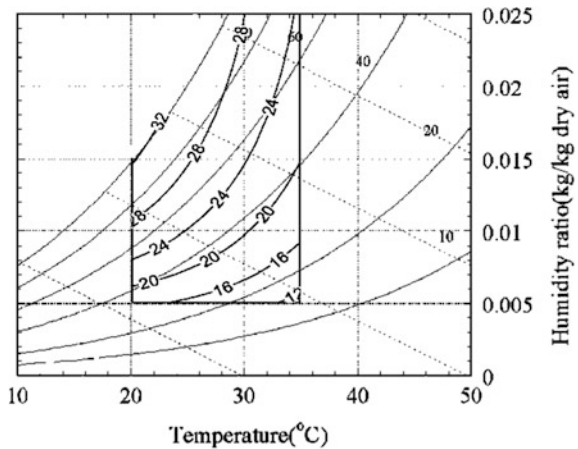
$R = 0.7$ , which suggests that a higher MRC is expected at  $R = 0.05$  at high regeneration temperatures. Compared to Fig. 2.27, Fig. 2.29 clearly shows this correlation between the MRC and water content difference.

It should be noted that unlike the present work, earlier works obtained an optimum isotherm shape on the condition of a fixed rotating speed and  $A_r/A_p$  for each regeneration temperature. This is why the earlier works found different optimum isotherm shapes. As was found in previous studies, if the same rotation speed and  $A_r/A_p$  are used for all  $R$  (for example, the optimal values for  $R = 1.0$ ), the adsorption capacity behavior shown in Fig. 2.30 is different from Fig. 2.27. In this case, the highest moisture removal capacity is found at the isotherm shape  $R = 0.4$ .

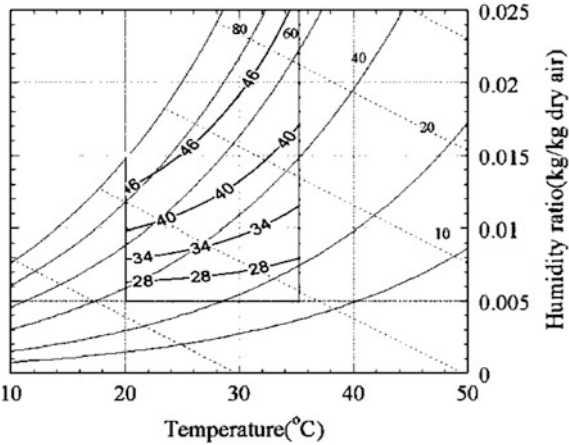


**Fig. 2.22** Profiles of the MRC as a function of the optimum wheel speed and  $A_r/A_p$  for the outdoor conditions  $T_{p,in} = 35^\circ\text{C}$  and  $\phi_{p,in} = 55\%$ ; **a**  $T_{r,in} = 60^\circ\text{C}$ , **b**  $T_{r,in} = 90^\circ\text{C}$ , **c**  $T_{r,in} = 120^\circ\text{C}$  and **d**  $T_{r,in} = 150^\circ\text{C}$  [12]

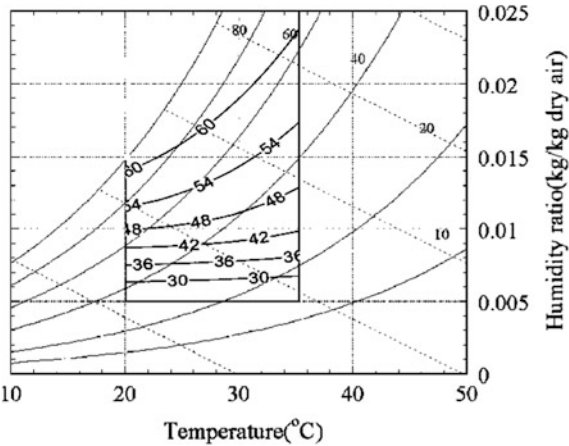
**Fig. 2.23** Psychrometric chart representation of the effect of the outdoor conditions on the MRC for  $T_{r,in} = 60^\circ\text{C}$  [12]



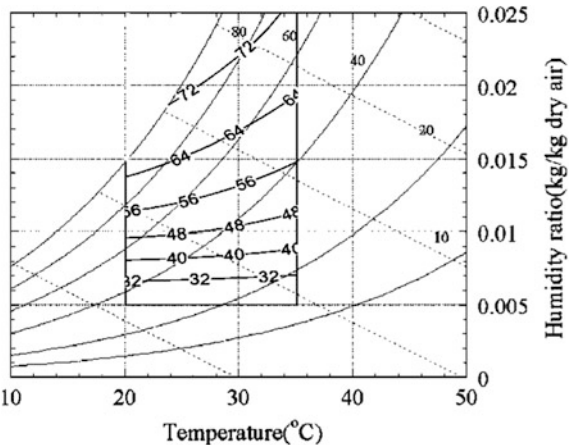
**Fig. 2.24** Psychrometric chart representation of the effect of the outdoor conditions on the MRC for  $T_{r,in} = 90\text{ }^{\circ}\text{C}$  [12]



**Fig. 2.25** Psychrometric chart representation of the effect of the outdoor conditions on the MRC for  $T_{r,in} = 120\text{ }^{\circ}\text{C}$  [12]



**Fig. 2.26** Psychrometric chart representation of the effect of the outdoor conditions on the MRC for  $T_{r,in} = 150\text{ }^{\circ}\text{C}$  [12]



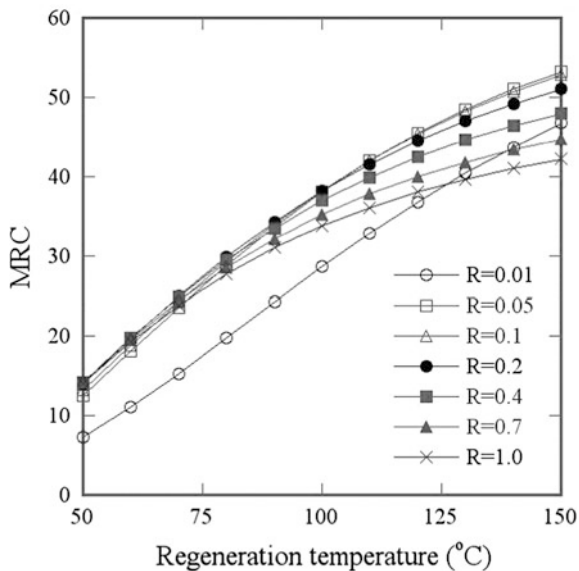


**Fig. 2.27** Variations of the MRC for various isotherm shapes and a range of regeneration temperatures from 50 to 150 °C. The MRC is evaluated at the optimal rotation speed and  $A_r/A_p$  of each isotherm shape at each regeneration temperature [54]

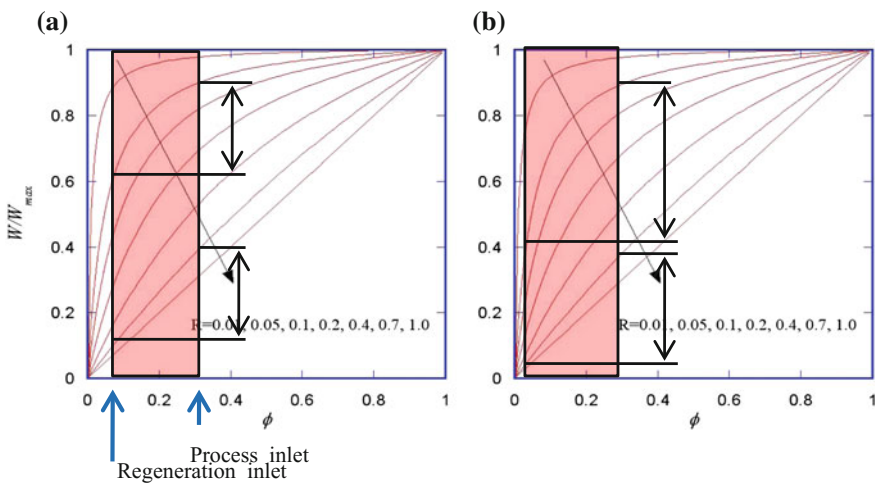


**Fig. 2.28** Typical example of water content differences evaluated by the process inlet and regeneration inlet conditions for the isotherm shapes of  $R = 0.05$  and  $R = 0.7$  at a **a** low regeneration temperature and **b** high regeneration temperature [54]



**Fig. 2.29** Variations of the water content difference evaluated by the process inlet and regeneration inlet conditions for various isotherm shapes and a range of regeneration temperature from 50 to 150 °C [54]

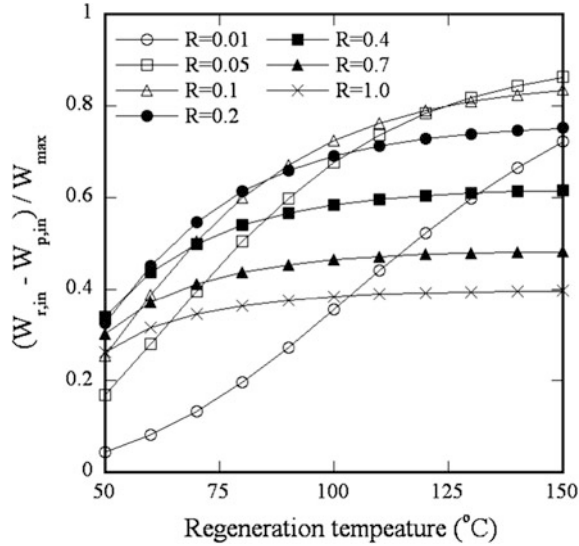
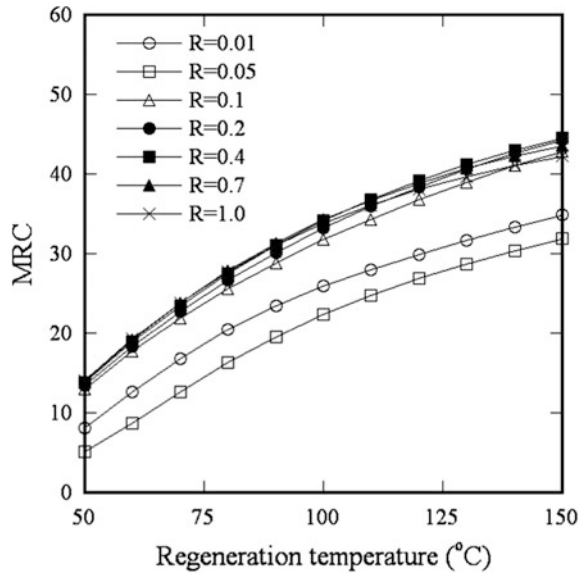


**Fig. 2.30** Variations of the MRC for various isotherm shapes and a range of regeneration temperature from 50 to 150 °C. The MRC is evaluated at the optimal rotation speed and  $A_r/A_p$  of  $R = 1.0$  at each regeneration temperature [54]



We can also find the sensitivity of the isotherm shape to the design parameters by comparing Figs. 2.15 and 2.16. The variation of optimal rotation speed is much higher than  $A_r/A_p$ .



### 2.3.5 Optimization

The system design of the desiccant cooling system poses a number of questions associated with a single parameter and/or their combinations. These include system components such as the sensible heat exchanger, regenerative evaporative cooler and desiccant wheel, as well as the operating conditions such as the outdoor conditions, regenerative temperature and rate of outdoor influx. The parameters related to the desiccant wheel, such as the wheel speed and the properties of the desiccant material, should be considered.

One of the methods for system optimization is the thermo-economic approach. This exergetic method was applied for the desiccant-evaporative air-conditioning system [65, 66], hybrid system [67, 68] and solar-desiccant air-conditioning system [69]. Enteria et al. [70] compared the different components of exergetic efficiency at the reference conditions of outdoor air.

It is a time-intensive task to examine the contribution of each component of the desiccant system and the contributions of the operating conditions because several parameters are involved in the performance of a desiccant cooling system. Therefore, it is impractical to evaluate each individual case using an exhaustive approach. In the present study, a numerical simulation has been conducted for 11 design parameters with 3 levels. The considered design parameters and its variations ( $\pm 30\%$  for the properties of the desiccant material and  $\pm 10\%$  for the others) are summarized in Table 2.5. It should be noted that the regeneration temperature is set at  $T_{10} = 75$ ,  $T_{10} = 60$  °C which is low enough to be acquired from low-density energy resources such as local heating, solar energy and waste heat. The base conditions for the desiccant material are from silica gel. The parameters related to the desiccant material are the mass fraction, heat capacity, density and maximum water uptake. Wheel performance dependency on these parameters is discussed by Chung et al. [40]. Wheel speed is set at 150 s/rev which is near the optimum wheel speed obtained in earlier work [12].

**Table 2.5** Base conditions and 3 levels of design parameters employed in the simulations [13]

Factor	Level		
	1 (%)	2 (base condition)	3 (%)
BP	-10	0.3	+10
$T_{\text{air}}$ [°C]	-10	35	+10
$\phi_{\text{air}}$ [%]	-10	40	+10
$\varepsilon_{\text{SHE}}$ [-]	-10	0.8	+10
$\varepsilon_{\text{REC}}$ [-]	-10	0.8	+10
$T_r$ [°C]	-30	75	+30
$t_p$ [s]	-30	75	+30
$f_d$ [-]	-30	0.75	+30
$c_{p,d}$ [J kg <sup>-1</sup> K <sup>-1</sup> ]	-30	921	+30
$\rho_d$ [kg m <sup>-3</sup> ]	-30	720	+30
$W_{\text{max}}$ [-]	-30	0.4	+30

Different system configurations have been proposed to achieve high system performance [2]. We confined our interest to only 2 cases in Fig. 2.31. The sensible heat exchanger acts as a pre-cooler after the desiccant and also as a preheater before

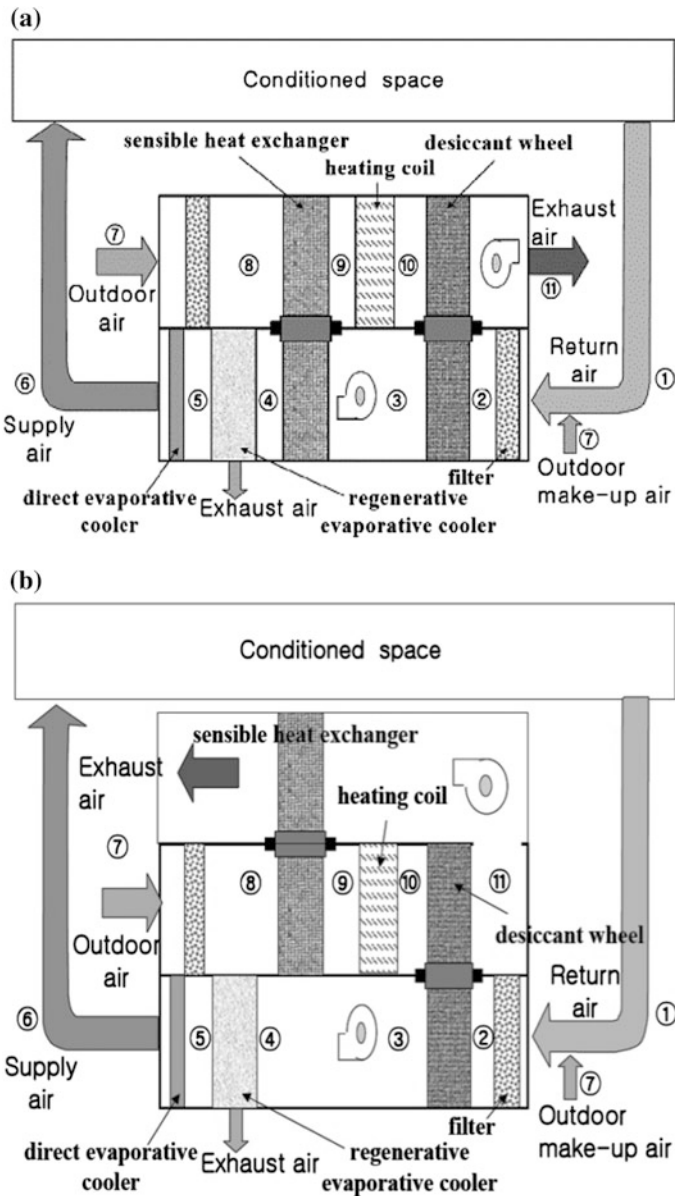


**Fig. 2.31** Schematics of the desiccant cooling system in **a** configuration A and **b** configuration B [13]

the regeneration section, which results in enhanced performance of the whole system. Conversely in system configuration B in Fig. 2.31b, the sensible heat exchanger fulfills the role of the preheater before the heating coil, which reduces the required energy for regeneration and results in enhanced performance. The performances of each system are compared. The desired indoor conditions is fixed at  $T_1 = 27\text{ }^\circ\text{C}$  and  $\phi_1 = 50\%$ . The 1:1 split between the regeneration and dehumidification sections of the desiccant wheel is assumed because the present work is focused on low regeneration temperatures.

The cooling performance of the REC can be represented by the cooling effectiveness, which is defined as:

$$\varepsilon_{\text{REC}} = \frac{T_{\text{h,in}} - T_{\text{h,out}}}{T_{\text{h,in}} - D_{\text{h,in}}} \quad (2.31)$$

where  $D_{\text{h,in}}$  is the inlet dew point temperature of the process air. It is the lowest outlet temperature that can be achieved in the REC. The base condition for  $\varepsilon_{\text{REC}}$  is 0.8.

The performance of the sensible heat exchanger can be evaluated by the following equations:

$$\varepsilon_{\text{SHE}} = \frac{T_9 - T_8}{T_3 - T_8} \quad \text{for system configuration A} \quad (2.32)$$

$$\varepsilon_{\text{SHE}} = \frac{T_9 - T_8}{T_{11} - T_8} \quad \text{for system configuration B} \quad (2.33)$$

The base condition for  $\varepsilon_{\text{SHE}}$  is 0.8.

The system performance is the object function for the analysis of variance (ANOVA) and can be evaluated using the amount of cooling capacity per unit air flow rate and/or the COP, which is defined as the ratio of the cooling capacity to the required energy for regeneration.

$$Q = (h_1 - h_6)(1 - BP) \quad (2.34)$$

$$\text{COP} = \frac{Q}{Q_r} \quad (2.35)$$

where the required energy for regeneration is obtained by  $Q_r = \dot{m}_p(h_{10} - h_9)t_r/t_p$ .

The orthogonal array L27 ( $3^{13}$ ) was adopted for the ANOVA [71] to find the optimal condition for each parameter and give the individual impact ratio of the system performance. The sum of the square is defined as  $ST = \sum x_{ij}^2 - (T^2/N)$ , where  $x$  is the value of the numerical experiment,  $T (= \sum x_{ij})$  is the summation of the numerical experiments, and  $N$  is the number of numerical experiments. We denote the degree of freedom by  $\phi$ , with the appropriate subscript  $i$  ( $=BP, T_{\text{air}}, \phi_{\text{air}}, \varepsilon_{\text{SHE}}, \varepsilon_{\text{REC}}, T_r, t_p, f_d, c_{p,d}, \rho_d, W_{\text{max}}$ ), which is defined as the level of factor  $i$  minus 1.

The mean square  $V$  is obtained by  $ST/\varphi$ . For a given level of significance, if  $F_0(= V_i/V_e)$  is greater than the corresponding  $F$ -distribution, (i.e.,  $F(\varphi_i, \varphi_e; \alpha)$ ), we say that factor  $i$  is significant, where  $\alpha$  represents the significance level.

If we chose the COP as the indicator of system performance, the results of the ANOVA are summarized in Tables 2.6 and 2.7 for the configurations A and B of the desiccant systems shown in Fig. 2.31. The  $F_0$  values of  $\varphi_{\text{air}}$  and  $\varepsilon_{\text{REC}}$  are 3.35 and 2.59, respectively, which is not small enough to be ignored in the case of a significance level of 5%. Therefore, we may consider that the factors  $\varphi_{\text{air}}$  and  $\varepsilon_{\text{REC}}$  are also slightly significant. Regardless of the system configuration, the contribution of  $BP$ ,  $\varepsilon_{\text{SHE}}$  and  $t_p$  and the parameters related to the desiccant material such as  $f_d$ ,  $c_{p,d}$ ,  $\rho_d$  and  $W_{\text{max}}$  are negligible, which may be surprising because it is believed that the desiccant material is one of the dominant factors related to the system performance. Recently, Faust et al. [72] developed a high-powered, SAP-based desiccant that can absorb 4–5 times more water than silica gel or zeolite, which showed clear system performance enhancement. We can conclude that more than  $\pm 30\%$  variations of the desiccant material properties are required for the development a new desiccant material to enhance the system performance.

After pooling the contribution of the negligible parameters, the contribution ratio of each factor is re-evaluated. The procedure is summarized in the ANOVA in Tables 2.6 and 2.7, which shows that the factors  $T_{\text{air}}$ ,  $\phi_{\text{air}}$ ,  $\varepsilon_{\text{REC}}$  and  $T_r$  are significant at the 5% level. Note that the values in parentheses are after pooling. The details of the procedure on the ANOVA can be found in Park [71]. The results provide a quantitative estimation of the various design parameters that affect the performance and help to determine the main factors for optimum design of a desiccant cooling system. The regeneration temperature is the most dominant parameter (31.9% for configuration A and 23.9% for system configuration B), and the outdoor conditions play a significant role in the performance of a desiccant cooling system (25.5 and 9% for  $T_{\text{air}}$  and  $\phi_{\text{air}}$ , respectively, for system configuration A and 20.6 and 8.7% for  $T_{\text{air}}$  and  $\phi_{\text{air}}$ , respectively, for system configuration B). These results are in line with the results of using the cooling capacity  $Q$  as the indicator of system performance. For reference, the results for system configuration A are given in Table 2.8.

If we assume that the errors are normally distributed, the  $100(1-\alpha)\%$  confidence interval on the  $t$ -distribution is:

$$\bar{y} \pm t\left(\varphi_e; \frac{\alpha}{2}\right) \sqrt{\frac{V_e}{n_e}} \quad (2.36)$$

where  $\varphi_e$  and  $V_e$  are the degree of freedom and mean square for error, respectively, and  $n_e$  denotes the effective number of replications that can be obtained from the relationship as is calculated as follows:

**Table 2.6** ANOVA for system configuration A when the COP is chosen as the indicator of system performance [13]

	BP	$T_{\text{air}}$	$\phi_{\text{air}}$	$\varepsilon_{\text{SHE}}$	$\varepsilon_{\text{REC}}$	$T_r$	$t_p$	$f_d$	$c_{p,d}$	$\rho_d$	$W_{\text{max}}$	e
Sum of squares	0.01724	0.33964	0.13678	0.00131	0.10569	0.41927	0.01921	0.01930	0.05303	0.00610	0.03354	0.08172(0.23145)
Degree of freedom	2	2	2	2	2	2	2	2	2	2	2	4(18)
Mean square	0.00862	0.16982	0.06839	0.00065	0.05284	0.20964	0.00960	0.00965	0.02652	0.00305	0.01677	0.02043(0.012858)
$F_0$ (before pooling)	0.42193	8.31197	3.3474	0.03199	2.58648	10.26078	0.47007	0.47226	1.29790	0.14927	0.82081	
$F_0$ (after pooling)		13.2069	5.31877		4.10972	16.30360						
Contribution ratio		0.255	0.09		0.065	0.319						0.271

**Table 2.7** ANOVA for system configuration B when the COP is chosen as the indicator of system performance [13]

	BP	$T_{\text{air}}$	$\varphi_{\text{air}}$	$\varepsilon_{\text{SHE}}$	$\varepsilon_{\text{REC}}$	$T_{\text{r}}$	$t_{\text{p}}$	$f_{\text{d}}$	$c_{\text{p,d}}$	$\rho_{\text{d}}$	$W_{\text{max}}$	e
Sum of squares	0.02027	0.28244	0.13621	0.03634	0.22273	0.32192	0.02512	0.00851	0.07827	0.03255	0.02632	0.03591 (0.26329)
Degree of freedom	2	2	2	2	2	2	2	2	2	2	2	4(18)
Mean square	0.01014	0.14122	0.06810	0.01817	0.11136	0.16096	0.01256	0.00426	0.03914	0.01627	0.01316	0.00898 (0.14627)
$F_0$ (before pooling)	1.12888	15.72880	7.585232	2.023568	12.40336	17.92703	1.39873	0.47391	4.358865	1.812563	1.46586	
$F_0$ (after pooling)		9.654592	4.6559381		7.613386	11.00390						
Contribution ratio		0.206	0.087		0.158	0.239						0.310

**Table 2.8** ANOVA for system configuration A when Q is chosen as the indicator of system performance [13]

	BP	$T_{air}$	$RH_{air}$	$e_{SHE}$	$e_{REC}$	$T_{reg}$	$\tau_{pro}$	$f_d$	$c_{p,d}$	$\rho_d$	$W_{max}$	e
Sum of squares	8.33292	337.44301	98.83324	5.03098	88.22058	749.5578	8.44539	28.60372	2.39312	14.2557	11.3134	19.22886(97.60410)
Degree of freedom	2	2	2	2	2	2	2	2	2	2	2	4(18)
Mean square	4.1665	168.7215	49.4166	2.5155	44.1103	374.7789	4.2227	14.3019	1.1966	7.1279	5.6567	4.8072(5.42245)
$F_0$ (before pooling)	0.8667	35.0976	10.2797	0.52327	9.1759	77.9617	0.8784	2.9751	0.2489	1.4827	1.1767	
$F_0$ (after pooling)		31.1154	9.11334		8.13475	69.1162						
Contribution ratio		0.238	0.064		0.056	0.539						0.103

$$n_e = \frac{n}{\sum \varphi_i + 1} \quad (2.37)$$

The optimum levels of the significant factors in system configuration A that maximize the COP are  $T_{\text{air},1}$ ,  $\phi_{\text{air},1}$ ,  $\varepsilon_{\text{REC},3}$  and  $T_{\text{r},1}$ . Note that the estimated COP at the optimum conditions is 0.9896 within the confidence interval  $1.0374 \pm 0.1375$ . The optimum levels of the significant factors in system configuration B are same as system configuration A, and the estimated COP at the optimum conditions is 1.28577, which is also within the confidence interval  $1.2042 \pm 0.1467$ .

To focus on the application of a district cooling system to utilize the over-supplied heat in summer season or a solar system using medium-temperature collectors, the regeneration temperature is fixed at a typical value of 75 °C. Additionally, the outdoor conditions are also fixed at  $T_7 = 35$  °C and  $\varphi_7 = 40\%$ , which are the typical summer conditions in Korea. For system configuration A, only the contributions of  $\varepsilon_{\text{REC},t_p,f_d}$  and  $\rho_d$  are meaningful. The most dominant parameter is  $\varepsilon_{\text{REC}}$ , whose contribution ratio to the system performance is 32.5%. General trends of the wheel parameters  $f_d$  and  $\rho_d$  are similar to earlier research by Chung et al. [40]; however, the analysis in Chung et al. [40] is confined to only wheel performance, i.e., the wheel performance is increased as  $f_d$  and  $\rho_d$  increase.

Contrary to system configuration A, the sensible heat exchanger plays a significant role in system configuration B, whose contribution ratio is estimated to be as high as 16.9%. The impact of the cooling performance of REC is also the most crucial factor in this configuration. This suggests that further research attention on regenerative evaporative cooler should be given to enhance the system performance. In this system configuration, the general trends of the wheel parameters  $f_d$ ,  $c_{p,d}$  and  $\rho_d$  are also similar to earlier research by Chung et al. [40].

## 2.4 Conclusions

Despite the advantage of being an eco-friendly refrigeration system driven by low-grade waste heat and separate control of sensible and latent cooling, widespread use of desiccant cooling systems is impaired by their relatively large size and low system performance. Numerous studies have focused on various aspects of the desiccant system, particularly the desiccant wheel, which is the most crucial component to enhance the system performance.

Mathematical modeling is a convenient approach to performing parametric research and optimization analysis of desiccant wheels with less time and cost than experimental methods. In addition, mathematical modeling can also provide the fundamental physics and intuition to develop new hybrid systems. However, mathematical modeling of desiccant wheels is a difficult task because the heat and mass transfer are coupled and too complicated to completely understand. Several mathematical models have been constructed and employed to analyze, develop and



design desiccant wheels. In this work, a brief review of mathematical modeling for the desiccant wheel is examined, and some typical issues, such as (i) channel geometry, (ii) adsorbent, (iii) isotherm, (iv) wheel speed, (v) regeneration temperature, (vi) area ratio of the regeneration to dehumidification section, (vii) sensitivity to outdoor weather conditions and (viii) optimizing the components of the desiccant system, are examined. The results of the case studies are also discussed.

Although significant advances have been made, in addition to the research issues mentioned above, the issues of newly developed hybrid system and new adsorbents still remain in the reliable and practical application of desiccant systems.

## References

1. Mazzei P, Minichiello F, Palma D (2005) HVAC dehumidification systems for thermal comfort: a critical review. *Appl Therm Eng* 25:677–707. doi:[10.1016/j.applthermaleng.2004.07.014](https://doi.org/10.1016/j.applthermaleng.2004.07.014)
2. Jani DB, Mishra M, Sahoo PK (2016) Solid desiccant air conditioning—a state of the art review. *Renew Sustain Energy Rev* 60:1451–1469. doi:[10.1016/j.rser.2016.03.031](https://doi.org/10.1016/j.rser.2016.03.031)
3. Mavroudaki P, Beggs CB, Sleight PA, Halliday SP (2002) The potential for solar powered single-stage desiccant cooling in southern Europe. *Appl Therm Eng* 22:1129–1140. doi:[10.1016/S1359-4311\(02\)00034-0](https://doi.org/10.1016/S1359-4311(02)00034-0)
4. Halliday S, Beggs C, Sleight P (2002) The use of solar desiccant cooling in the UK: a feasibility study. *Appl Therm Eng* 22:1327–1338. doi:[10.1016/S1359-4311\(02\)00052-2](https://doi.org/10.1016/S1359-4311(02)00052-2)
5. Hong SW, Kwon OK, Chung JD (2016) Application of an embossed plate heat exchanger to adsorption chiller. *Int J Refrig* 65:142–153. doi:[10.1016/j.ijrefrig.2016.02.012](https://doi.org/10.1016/j.ijrefrig.2016.02.012)
6. Dai Y, Wang R, Zhang H, Yu J (2001) Use of liquid desiccant cooling to improve the performance of vapor compression air conditioning. *Appl Therm Eng* 21:1185–1202. doi:[10.1016/S1359-4311\(01\)00002-3](https://doi.org/10.1016/S1359-4311(01)00002-3)
7. Mazzei P, Minichiello F, Palma D (2002) Desiccant HVAC systems for commercial buildings. *Appl Therm Eng* 22:545–560. doi:[10.1016/S1359-4311\(01\)00096-5](https://doi.org/10.1016/S1359-4311(01)00096-5)
8. George OGL, Gerald C, Thomas B (1988) Performance of a solar desiccant cooling system. *J Sol Energy Eng* 110:165–171
9. Collier RKC (1991) An analytic investigation of methods for improving the performance of desiccant cooling system. *ASME J Sol Energy Sci Eng* 113:157–163
10. Zheng W, Worek WM, Novosel D (1995) Performance optimization of rotary dehumidifiers. *J Sol Energy Eng* 117:40–44
11. Dai YJ, Wang RZ, Zhang HF (2001) Parameter analysis to improve rotary desiccant dehumidification using a mathematical model. *Int J Therm Sci* 40:400–408. doi:[10.1016/S1290-0729\(01\)01224-8](https://doi.org/10.1016/S1290-0729(01)01224-8)
12. Chung JD, Lee D-YY, Yoon SM (2009) Optimization of desiccant wheel speed and area ratio of regeneration to dehumidification as a function of regeneration temperature. *Sol Energy* 83:625–635. doi:[10.1016/j.solener.2008.10.011](https://doi.org/10.1016/j.solener.2008.10.011)
13. Chung JD, Lee DY (2011) Contributions of system components and operating conditions to the performance of desiccant cooling systems. *Int J Refrig* 34:922–927. doi:[10.1016/j.ijrefrig.2011.03.003](https://doi.org/10.1016/j.ijrefrig.2011.03.003)
14. Kodama A, Hirayama T, Goto M, Hirose T, Critoph RE (2001) The use of psychrometric charts for the optimisation of a thermal swing desiccant wheel. *Appl Therm Eng* 21:1657–1674. doi:[10.1016/S1359-4311\(01\)00032-1](https://doi.org/10.1016/S1359-4311(01)00032-1)
15. Cui Q, Chen H, Tao G, Yao H (2005) Performance study of new adsorbent for solid desiccant cooling. *Energy* 30:273–279. doi:[10.1016/j.energy.2004.05.006](https://doi.org/10.1016/j.energy.2004.05.006)

16. Jia CX, Dai YJ, Wu JY, Wang RZ (2006) Experimental comparison of two honeycombed desiccant wheels fabricated with silica gel and composite desiccant material. *Energy Convers Manage* 47:2523–2534. doi:[10.1016/j.enconman.2005.10.034](https://doi.org/10.1016/j.enconman.2005.10.034)
17. White SD, Goldsworthy M, Reece R, Spillmann T, Gorur A, Lee DY (2011) Characterization of desiccant wheels with alternative materials at low regeneration temperatures. *Int J Refrig* 1786–1791
18. Hong SW, Ahn SH, Chung JD, Bae KJ, Cha DA, Kwon OK (2016) Characteristics of FAM-Z01 compared to silica gels in the performance of an adsorption bed. *Appl Therm Eng* 104:24–33. doi:[10.1016/j.applthermaleng.2016.05.058](https://doi.org/10.1016/j.applthermaleng.2016.05.058)
19. Mittal V, Khan BK (2010) Experimental investigation on desiccant air-conditioning system in India. *Front Energy Power Eng China* 4:161–165. doi:[10.1007/s11708-009-0070-5](https://doi.org/10.1007/s11708-009-0070-5)
20. Zheng W, Worek WM (1993) Numerical simulation of combined heat and mass transfer processes in a rotary dehumidifier. *Numer Heat Transf Part A Appl* 23:211–232. doi:[10.1080/10407789308913669](https://doi.org/10.1080/10407789308913669)
21. Zhang LZ, Niu JL (2002) Performance comparisons of desiccant wheels for air dehumidification and enthalpy recovery. *Appl Therm Eng* 22:1347–1367. doi:[10.1016/S1359-4311\(02\)00050-9](https://doi.org/10.1016/S1359-4311(02)00050-9)
22. Zhang XJ, Dai YJ, Wang RZ (2003) A simulation study of heat and mass transfer in a honeycombed rotary desiccant dehumidifier. *Appl Therm Eng* 23:989–1003. doi:[10.1016/S1359-4311\(03\)00047-4](https://doi.org/10.1016/S1359-4311(03)00047-4)
23. Ahmed MHH, Kattab NMM, Fouad M (2005) Evaluation and optimization of solar desiccant wheel performance. *Renew Energy* 30:305–325. doi:[10.1016/j.renene.2004.04.010](https://doi.org/10.1016/j.renene.2004.04.010)
24. Liu Y, Wang R (2003) Pore structure of new composite adsorbent  $\text{SiO}_2 \cdot x\text{H}_2\text{O} \cdot y\text{CaCl}_2$  with high uptake of water from air. *Sci China Ser E: Technol Sci* 46:551–559. doi:[10.1360/02ye0480](https://doi.org/10.1360/02ye0480)
25. Maclaine-cross IL (1985) High-performance adiabatic desiccant open-cooling cycles. *J Sol Energy Eng* 107:102–104
26. Henning HM (2007) Solar assisted air conditioning of buildings—an overview. *Appl Therm Eng* 27:1734–1749. doi:[10.1016/j.applthermaleng.2006.07.021](https://doi.org/10.1016/j.applthermaleng.2006.07.021)
27. Worek WM, Zheng W, Belding WA, Novosel D, Holeman WD (1991) Simulation of advanced gas-fired desiccant cooling systems. *Ashrae Trans* 4:609–614
28. Ge TS, Li Y, Wang RZ, Dai YJ (2008) A review of the mathematical models for predicting rotary desiccant wheel. *Renew Sustain Energy Rev* 12:1485–1528. doi:[10.1016/j.rser.2007.01.012](https://doi.org/10.1016/j.rser.2007.01.012)
29. Charoensupaya D, Worek WM (1988) Parametric study of an open-cycle adiabatic, solid, desiccant cooling system. *Energy* 13:739–747. doi:[10.1016/0360-5442\(88\)90106-5](https://doi.org/10.1016/0360-5442(88)90106-5)
30. Sphaier LA, Worek WM (2006) Comparisons between 2-D and 1-D Formulations of Heat and Mass Transfer in Rotary Regenerators. *Numer Heat Transf Part B Fundam* 49:223–237. doi:[10.1080/10407790500434166](https://doi.org/10.1080/10407790500434166)
31. Ahn SH, Hong SW, Kwon OK, Chung JD (2013) Validity of inter-particle models for the mass transfer kinetics of a fin tube type adsorption bed. *Korea J Air-Conditioning Refrig Eng* 25:660–667
32. Hong SW, Ahn SH, Kwon OK, Chung JD (2014) Validity of intra-particle models of mass transfer kinetics in the analysis of a fin-tube type adsorption bed. *J Mech Sci Technol* 28:1985–1993. doi:[10.1007/s12206-014-0347-4](https://doi.org/10.1007/s12206-014-0347-4)
33. Yamamoto E, Katsurayama K, Watanabe F, Matsuda H, Hasatani M (2000) Heat and mass transfer characteristics in adsorption of water vapor for silica gel packed bed adsorber. *J Chem Eng Jpn* 33:12–18. doi:[10.1252/jcej.33.12](https://doi.org/10.1252/jcej.33.12)
34. Watanabe F, Watabe Y, Katsuyama H, Kozuka J, Hasatani M, Marumo C (1993) Heat transfer accompanied by adsorption/desorption of water vapour in adsorption heat pump of packed bed type. *Kagaku Kogaku Ronbunshu* 19:83–90. doi:[10.1252/kakoronbunshu.19.83](https://doi.org/10.1252/kakoronbunshu.19.83)
35. Li J, Kubota M, Watanabe F, Kobayashi N, Hasatani M (2004) Optimal design of a fin-type silica gel tube module in the silica gel/water adsorption heat pump. *J Chem Eng Jpn* 37:551–557. doi:[10.1252/jcej.37.551](https://doi.org/10.1252/jcej.37.551)

36. Yadav A, Bajpai VK (2011) Optimization of operating parameters of desiccant wheel for rotation speed. *Int J Adv Sci Techno* 32:109–116
37. Gao Z, Mei VC, Tomlinson JJ (2005) Theoretical analysis of dehumidification process in a desiccant wheel. *Heat Mass Transf* 41:1033–1042. doi:[10.1007/s00231-005-0663-4](https://doi.org/10.1007/s00231-005-0663-4)
38. Zhang LZ, Niu JL (2001) A numerical study of laminar forced convection in sinusoidal ducts with arc lower boundaries under uniform wall temperature. *Numer Heat Transf Part A Appl* 40:55–72. doi:[10.1080/10407780117998](https://doi.org/10.1080/10407780117998)
39. Al-Sharqawi HS, Lior N (2008) Effect of flow-duct geometry on solid desiccant dehumidification. *Ind Eng Chem Res* 47:1569–1585. doi:[10.1021/ie0707319](https://doi.org/10.1021/ie0707319)
40. Chung DJ, Lee D, Yoon SM (2010) Effect of parameters related to channel and desiccant on the size of desiccant rotor. *Int J Air-Conditioning Refrig* 18:201–211. doi:[10.1142/S2010132510000125](https://doi.org/10.1142/S2010132510000125)
41. Llano-Restrepo M, Mosquera MA (2009) Accurate correlation, thermochemistry, and structural interpretation of equilibrium adsorption isotherms of water vapor in zeolite 3A by means of a generalized statistical thermodynamic adsorption model. *Fluid Phase Equilib* 283:73–88. doi:[10.1016/j.fluid.2009.06.003](https://doi.org/10.1016/j.fluid.2009.06.003)
42. Eicker U, Schürger U, Köhler M, Ge T, Dai Y, Li H, Wang R (2012) Experimental investigations on desiccant wheels. *Appl Therm Eng* 42:71–80. doi:[10.1016/j.applthermaleng.2012.03.005](https://doi.org/10.1016/j.applthermaleng.2012.03.005)
43. Kim YD, Thu K, Ng KC (2014) Adsorption characteristics of water vapor on ferroaluminophosphate for desalination cycle. *Desalination* 344:350–356. doi:[10.1016/j.desal.2014.04.009](https://doi.org/10.1016/j.desal.2014.04.009)
44. Saha BB, El-Sharkawy II, Chakraborty A, Koyama S (2007) Study on an activated carbon fiber-ethanol adsorption chiller: part I—system description and modelling. *Int J Refrig* 30:86–95. doi:[10.1016/j.ijrefrig.2006.08.004](https://doi.org/10.1016/j.ijrefrig.2006.08.004)
45. Li A, Bin Ismail A, Thu K, Ng KC, Loh WS (2014) Performance evaluation of a zeolite–water adsorption chiller with entropy analysis of thermodynamic insight. *Appl Energy* 130:702–711. doi:[10.1016/j.apenergy.2014.01.086](https://doi.org/10.1016/j.apenergy.2014.01.086)
46. Collier RK, Cale TS, Lavan Z (1986) Advanced desiccant materials assessment. Final report, February 1985–May 1986. United States
47. Banks PJ (1985) Prediction of heat and mass regenerator performance using nonlinear analogy method: part 2—comparison of methods. *J Heat Transf* 107:230–238
48. Banks PJ (1985) Prediction of Heat and Mass Regenerator Performance Using Nonlinear Analogy Method: Part 1—Basis. *J Heat Transfer* 107:222–229
49. Lee G, Lee D-Y, Kim MS (2004) Development of a linearized model and verification of the exact solution for the analysis of a desiccant dehumidifier. *J Air-Conditioning Refrig Eng* 811–819
50. Kim D, Choi Y, Lee D (2011) Development of a simple analytical model for desiccant wheels-I. Approximate solution of the governing equations. *Korean J Air-Conditioning Refrig Eng* 23:821–827
51. Lee DY, Kim DS (2014) Analytical modeling of a desiccant wheel. *Int J Refrig* 42:97–111. doi:[10.1016/j.ijrefrig.2014.02.003](https://doi.org/10.1016/j.ijrefrig.2014.02.003)
52. Cejudo J, Moreno R, Carrillo A (2002) Physical and neural network models of a silica-gel desiccant wheel. *Energy Build* 34:837–844. doi:[10.1016/S0378-7788\(02\)00100-7](https://doi.org/10.1016/S0378-7788(02)00100-7)
53. Golubovic MN, Worek WM (2004) Influence of elevated pressure on sorption in desiccant wheels. *Numer Heat Transf Part A Appl* 45:869–886. doi:[10.1080/10407780490439068](https://doi.org/10.1080/10407780490439068)
54. Chung JD, Lee D-Y (2009) Effect of desiccant isotherm on the performance of desiccant wheel. *Int J Refrig* 32:720–726. doi:[10.1016/j.ijrefrig.2009.01.003](https://doi.org/10.1016/j.ijrefrig.2009.01.003)
55. Ruivo CR, Costa JJ, Figueiredo AR (2006) Analysis of simplifying assumptions for the numerical modeling of the heat and mass transfer in a porous desiccant medium. *Numer Heat Transf Part A Appl* 49:851–872. doi:[10.1080/10407780500483552](https://doi.org/10.1080/10407780500483552)
56. Ruivo CR, Costa JJ, Figueiredo AR (2008) On the validity of lumped capacitance approaches for the numerical prediction of heat and mass transfer in desiccant airflow systems. *Int J Therm Sci* 47:282–292. doi:[10.1016/j.ijthermalsci.2007.01.032](https://doi.org/10.1016/j.ijthermalsci.2007.01.032)

57. Sphaier LA, Worek WM (2004) Analysis of heat and mass transfer in porous sorbents used in rotary regenerators. *Int J Heat Mass Transf* 47:3415–3430. doi:[10.1016/j.ijheatmasstransfer.2004.01.016](https://doi.org/10.1016/j.ijheatmasstransfer.2004.01.016)
58. Pesaran AA, Mills A (1984) Modeling of solid-side transfer in desiccant particle beds. In: *Proceedings of 6th Annual ASME Solar Energy Division Conference*. New York
59. Harshe YM, Utikar RP, Ranade VV, Pahwa D (2005) Modeling of rotary desiccant wheels. *Chem Eng Technol* 28:1473–1479. doi:[10.1002/ceat.200500164](https://doi.org/10.1002/ceat.200500164)
60. Pesaran AA, Mills AF (1987) Moisture transport in silica gel packed beds—I. Theoretical study. *Int J Heat Mass Transf* 30:1037–1049. doi:[10.1016/0017-9310\(87\)90034-2](https://doi.org/10.1016/0017-9310(87)90034-2)
61. Pesaran AA (1983) Moisture transport in silica gel particle beds. [DESSICANT]. University of California, Los Angeles
62. Kakaç S, Shah RK, Aung W (1987) *Handbook of single-phase convective heat transfer*. Wiley, New York
63. ASHRAE (1998) Standard 139-1998. Method of testing for rating desiccant dehumidifiers utilizing heat for the regeneration process. ASHRAE, Inc, Atlanta
64. Simonson CJ, Besant RW (1999) Energy wheel effectiveness: part II—correlations. *Int J Heat Mass Transf* 42:2171–2185. doi:[10.1016/S0017-9310\(98\)00327-5](https://doi.org/10.1016/S0017-9310(98)00327-5)
65. Kanoğlu M, Özdiñ Çarpınloğlu M, Yıldırım M (2004) Energy and exergy analyses of an experimental open-cycle desiccant cooling system. *Appl Therm Eng* 24:919–932. doi:[10.1016/j.applthermaleng.2003.10.003](https://doi.org/10.1016/j.applthermaleng.2003.10.003)
66. La D, Li Y, Dai YJ, Ge TS, Wang RZ (2012) Development of a novel rotary desiccant cooling cycle with isothermal dehumidification and regenerative evaporative cooling using thermodynamic analysis method. *Energy* 44:778–791. doi:[10.1016/j.energy.2012.05.016](https://doi.org/10.1016/j.energy.2012.05.016)
67. Pons M, Kodama A (2000) Entropic analysis of adsorption open cycles for air conditioning. Part 1: first and second law analyses. *Fuel Energy Abstr* 41:321. doi:[http://dx.doi.org/10.1016/S0140-6701\(00\)96820-6](http://dx.doi.org/10.1016/S0140-6701(00)96820-6)
68. Hürdoğan E, Büyükalaca O, Hepbaslı A, Yılmaz T (2011) Exergetic modeling and experimental performance assessment of a novel desiccant cooling system. *Energy Build* 43:1489–1498. doi:[10.1016/j.enbuild.2011.02.016](https://doi.org/10.1016/j.enbuild.2011.02.016)
69. Enteria N, Yoshino H, Takaki R, Mochida A, Satake A, Yoshie R (2013) Effect of regeneration temperatures in the exergetic performances of the developed desiccant-evaporative air-conditioning system. *Int J Refrig* 36:2323–2342. doi:[10.1016/j.ijrefrig.2013.08.005](https://doi.org/10.1016/j.ijrefrig.2013.08.005)
70. Enteria N, Yoshino H, Mochida A, Satake A, Takaki R (2015) Exergoeconomic performances of the desiccant-evaporative air-conditioning system at different regeneration and reference temperatures. *Int J Refrig* 56:81–98. doi:[10.1016/j.ijrefrig.2014.11.007](https://doi.org/10.1016/j.ijrefrig.2014.11.007)
71. Park SH (1996) *Robust design and analysis for quality engineering*. Chapman & Hall, London
72. Faust S, Guido F, Lee D (2007) Desiccant element and manufacturing method of the same. Korea Patent 0704235

Desiccant Heating, Ventilating, and Air-Conditioning  
Systems

Enteria, N.; Awbi, H.; Yoshino, H. (Eds.)

2017, X, 326 p. 181 illus., 138 illus. in color., Hardcover

ISBN: 978-981-10-3046-8